RSMC Tokyo – Typhoon Center

Technical Review

No. 10

Contents

Japan Meteorological Agency

March 2008

PREFACE

The RSMC Tokyo - Typhoon Center provides various tropical cyclone information products to National Meteorological and Hydrological Services (NMHSs) on a real-time basis in order to support tropical cyclone forecasting as well as disaster preparedness and prevention activities. The Center also offers publications such as *RSMC Tropical Cyclone Best Track* and *Annual Report on the Activities of the RSMC Tokyo - Typhoon Center* every year. In addition to these regular publications, the Center occasionally publishes *Technical Review* to outline the achievements of research and development on operational meteorological services for tropical cyclones.

This issue of *Technical Review* covers three topics relating to tropical cyclone analysis using satellite image data. These are: 1) Revision of JMA's Early Stage Dvorak Analysis and Its Use to Analyze Tropical Cyclones in the Early Developing Stage, 2) The Possibility of Determining Whether Organized Cloud Clusters Will Develop into Tropical Storms by Detecting Warm Core Structures from Advanced Microwave Sounding Unit Observations, and 3) Analysis of Tropical Cyclones Using Microwave Satellite Imagery.

The first of these explains the new diagnosis of T-number 0.5 in JMA's Early Stage Dvorak Analysis (EDA) and its use in judging tropical depressions. The second describes an investigation concerning the air temperature profiles of organized cloud clusters using advanced microwave sounding unit observations. A certain value and spatial size of positive temperature anomaly (a warm core) at an upper-troposphere level was found for clusters developing into tropical storms (TSs) in a number of cases. The third topic explains the use of microwave satellite imagery to analyze the inner structures and center positions of tropical cyclones. The method is used in tropical cyclone analysis at the Center to improve the accuracy of center positions estimated by the Dvorak method.

The RSMC Tokyo - Typhoon Center hopes this research will serve as useful reference toward the improvement of tropical cyclone forecasting and the mitigation of typhoon-related disasters.

Revision of JMA's Early Stage Dvorak Analysis and Its Use to Analyze Tropical Cyclones in the Early Developing Stage

Kenji KISHIMOTO

National Typhoon Center, Japan Meteorological Agency

Abstract

This report follows Kishimoto et al. (2007). The Japan Meteorological Agency (JMA) conducted verification of the behaviors of past tropical cyclones (TCs) for the purpose of developing the diagnosis of T-number 0.5 (T0.5). The results indicate that T0.5 diagnosis is valid for satellite image analysis for TCs in the early developing stage (early stage Dvorak analysis: EDA). Organized convective cloud systems (OCCSs) diagnosed as T0.0 or T0.5 can be recognized as follows:

- Most OCCSs are not yet determined as tropical depressions (TDs) when they are first diagnosed as T0.0.
- OCCSs are likely to be determined as TDs when they are first diagnosed as T0.5.

In summer 2007, based on the above results and Kishimoto et al. (2007), JMA revised EDA. The main part of this revision involved the addition of T0.5 diagnosis to the former EDA, which consisted of OCCS detection, T1.0 diagnosis and T1.5/2.0 diagnosis. In addition, JMA revised the criteria for determining the TC grade using EDA results. Analysis of TCs in the early developing stage using the revised EDA is explained through the example of the TD that became USAGI (0705).

1. Introduction

Since 2001, the Japan Meteorological Agency (JMA) has been operating satellite image analyses for tropical cyclones (TCs) in the early developing stage (referred to below as *early stage Dvorak analysis* (EDA)). Kishimoto et al. (2007) verified the validity of EDA for TC analysis[1] in the early developing stage, comparing EDA results with JMA's TC analysis data over the five-year period from 2002 to 2006. Following the above study, JMA conducted a verification of past TC behavior for the purpose of developing the diagnosis of T-number 0.5 (T0.5). In summer 2007, based on these two verification results, JMA revised EDA and started its operational use for analysis of TCs in the early developing stage.

Section 2 describes T0.5 diagnosis and its verification results, and the revision of EDA is introduced in Section 3. Analysis of TCs in the early developing stage using the revised EDA is presented in Section 4, and Section 5 outlines the conclusion.

[1] Refer to Section 2.1 of Kishimoto et al. (2007) for JMA's TC analysis.

2. Verification study for developing T0.5 diagnosis

2.1 T0.5 Diagnosis

T0.5 diagnosis is conducted in the process of the T1.0 diagnosis proposed by Tsuchiya et al. (2000, 2001). Table 2.1 shows the five features of an organized convective cloud system (OCCS)[2] with an intensity of T1.0. In this diagnosis, an OCCS is diagnosed as T0.0 when it satisfies less than four of these features, and is T0.5 when it satisfies four features.

Table 2.1 Features of OCCSs diagnosed as T1.0

The figure on the right illustrates an OCCS diagnosed as T1.0.

	Tsuchiya et al. (2000, 2001)
1	A convective cloud system has persisted for 12 hours or more.
2	The cloud system has a CSC defined within a diameter of 2.5° latitude or less.
3	The CSC has persisted for six hours or more.
4	The cloud system has an area of dense, cold (-31°C or colder) that appears less than 2° latitude from the center.
5	The above overcast is more than 1.5° latitude in diameter.

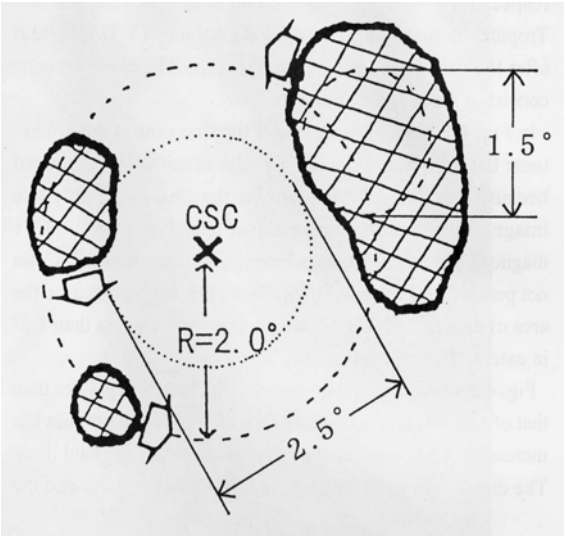

2.2 Verification

First, T0.5 diagnosis was experimentally conducted using EDA data from 2002 to 2006. The results were then compared with TCs on JMA's surface weather charts to verify the following points in the same way as in Kishimoto et al. (2007)[3]:

- Development of OCCSs diagnosed as T0.0 (T0.0-OCCSs) or T0.5 (T0.5-OCCSs) to TCs
- Timing of the first diagnosis of OCCSs as T0.0 (FDT0.0) or T0.5 (FDT0.5) and their development to TCs.

Table 2.2 shows the TC grades used for the verification; tropical depression for which no warning was issued (NTD), tropical depression for which warnings were issued (WTD) and tropical storm (TS).

---

[2] An OCCS is defined in this paper as a convective cloud system with a cloud system center (CSC). CSCs are explained in Section 2.2 of Kishimoto et al. (2007).

[3] Refer to Section 3.1 of Kishimoto et al. (2007) for details of the verification.

Table 2.2 TC grades used for the study

NTD	TCs with definite cyclonic surface wind circulation and max. winds of less than Force 7 on the Beaufort scale (less than 28 kt)
WTD	TCs with definite cyclonic surface wind circulation and max. winds of Force 7 (28-33 kt)
TS	TCs with definite cyclonic surface wind circulation and max. winds of Force 8 or 9 (34-47 kt)

Table 2.3 shows the percentages of T0.0- or T0.5-OCCSs that developed to NTDs, WTDs or TSs, and the average periods from FDT0.0 or FDT0.5 to the first determination as TSs (FDTS). This table also shows those of T1.0-, T1.5- and T2.0-OCCSs for comparison.

It indicates the following:

- The percentages of T0.0- and T0.5-OCCSs that developed to TSs were 26% and 35% respectively. The percentage for T0.5-OCCSs was higher than that for T0.0.
- The average periods from FDT0.0 and FDT0.5 to FDTS were 2.4 and 2.1 days respectively. These results correspond closely to the model for TC development shown by Dvorak (1984).

The results suggest that T0.5 diagnosis is valid for EDA.

Table 2.3 Percentages of T0.0- and T0.5-OCCSs that developed to NTDs, WTDs and TSs, and the average periods from FDT0.0 and FDT0.5 to FDTS from 2002 to 2006
Values for T1.0, T1.5 and T2.0 shown by Kishimoto et al. (2007) are included for comparison.

T-number	Number of OCCSs	Percentage (%) of OCCSs that reached each class			Average period (days) from first diagnosis as each T-number to the first determination as TSs (FDTS)
		NTD	WTD	TS	
T0.0	363	45	34	26	2.4
T0.5	267	64	47	35	2.1
T1.0	188	89	78	61	1.4
T1.5	112	97	95	79	0.8
T2.0	41	100	100	98	0.4

Table 2.4 shows the percentages of OCCSs that developed to NTDs or WTDs before, at and after FDT0.0 and FDT0.5, as well as the values for FDT1.0, FDT1.5 and FDT2.0 for comparison. It indicates the following:

- Few (4%) OCCSs were determined as NTDs before FDT0.0, while a significant number (24%) were determined as NTDs before FDT0.5.
- Few (5%) OCCSs were determined as WTDs before FDT0.5.

These results suggest that OCCSs are likely to be determined as NTDs at FDT0.5 in many cases.

Table 2.4 Percentages of OCCSs that developed to NTDs and WTDs before, at and after the first diagnosis as T0.0 and T0.5 from 2002 to 2006.
The values for T1.0, T1.5 and T2.0 shown by Kishimoto et al. (2007) are included for comparison.

T-number	Number of OCCSs	Percentage (%)					
		NTD			WTD		
		before	at	after	before	at	after
0.0	363	4	11	30	1	1	32
0.5	267	24	8	33	5	3	39
1.0	188	40	34	15	11	19	47
1.5	112	84	13	1	42	38	14
2.0	41	100	0	0	81	17	2

3. Revision of EDA

The main part of the revision involves the addition of T0.5 diagnosis to the former EDA[4], which consisted of OCCS detection, T1.0 diagnosis and T1.5/2.0 diagnosis. In addition, JMA revised the criteria for determining the TC grade using the verification results shown in Tables 2.3 and 2.4. Table 3.1 shows the criteria for determining the TC grade using T-numbers diagnosed through the new EDA compared to those diagnosed with the previous version. The criteria are based on the likelihood of OCCSs being determined as NTDs or WTDs at the time and the possibility of their development to TS status in the future. The former is prepared using the percentages of OCCSs that developed to NTDs or WTDs before or at their first diagnosis as the T-numbers in Table 2.4. The terms *unlikely*, *likely* and *highly likely* indicate percentages of lower than 30%, 30 to 70% and higher than 70% respectively. The latter is prepared using the percentages of OCCSs that developed to TSs in Table 2.3. The terms *poor*, *fair* and *high* indicate percentages of lower than 40%, 40 to 70% and higher than 70% respectively.

[4] Refer to Section 2.2 of Kishimoto et al. (2007) for the former EDA.

Table 3.1 Criteria for the determination of TC grade using T-numbers diagnosed through the new EDA compared to those diagnosed through the old EDA

<table>
<tr><td></td><td colspan="3">New EDA</td><td>Old EDA</td></tr>
<tr><td>T-number</td><td>Likelihood of being determined as NTDs at the time</td><td>Likelihood of being determined as WTDs at the time</td><td>Possibility of development to TSs in the future</td><td>Possibility of development to TSs in the future</td></tr>
<tr><td>0.0</td><td>Unlikely</td><td rowspan="2">Unlikely</td><td rowspan="2">Poor</td><td rowspan="2">Poor</td></tr>
<tr><td>0.5</td><td>Likely</td></tr>
<tr><td>1.0</td><td rowspan="3">Highly likely</td><td>Likely</td><td>Fair</td><td rowspan="3">High</td></tr>
<tr><td>1.5</td><td rowspan="2">Highly likely</td><td rowspan="2">High</td></tr>
<tr><td>2.0</td></tr>
</table>

4. Analysis of TCs in the early developing stage using the revised EDA

In order to analyze TCs in the early developing stage, JMA firstly diagnoses their T-number through the revised EDA and then determines their TC grade using the T-number, surface observation data, QuikSCAT data and numerical weather prediction (NWP) data in a comprehensive manner. As an example, analyses of the TD that became USAGI (0705) are described in Section 4.1.

4.1 Analyses of the pre-USAGI (0705) TC

An OCCS was initially detected at 00 UTC on 27 July 2007. It developed to a WTD at 18 UTC the same day, and was expected to develop to a TS within 24 hours (ExpT) at 06 UTC the next day. It then developed to a TS and was designated the name USAGI at 06 UTC on 29 July.

Figures 4.1, 4.2 and 4.3 show Asia-Pacific surface analyses (ASAS) and satellite images onto which the cloud system center (CSC) of the OCCS, NWP's surface winds and isobars are superimposed. The images represent 00 UTC on 27 July, 18 UTC on 27 July and 06 UTC on 28 July respectively. Figure 4.4 shows composites of satellite images and QuikSCAT data at 19 UTC on 27 July and 09 UTC on 28 July. All figures and data here are based on operational data rather than post-analysis data.

00 UTC, 27 July (Figure 4.1)

After 18 UTC on 26 July, a convective cloud system developed rapidly. At 00 UTC the next day, this cloud system was detected as an OCCS and satisfied four of the features (excluding the third) in Table 2.1, resulting in T0.5 status. This meant that the cloud system was likely to be determined as an NTD. In this case, it was determined as a low pressure area (LPA)[5] in ASAS since there were no available data to diagnose its TC grade except the EDA result.

At 06 UTC and 12 UTC the same day, the OCCS was also diagnosed as T0.5, since there were no data to confirm its development to a TC except the EDA result. It remained an LPA in ASAS.

18 UTC, 27 July (Figure 4.2, Figure 4.4 (a))

At 18 UTC on 27 July, the OCCS satisfied all five features and was diagnosed as T1.0. This result meant that the cloud system was highly likely to be determined as an NTD and likely to be determined as a WTD. In this case, the system was determined as a WTD in ASAS, since the latest NWP data presented a corresponding cyclone and also indicated signs of development. QuikSCAT data without rain flags indicated winds of over 25 kt around it at 19 UTC the same day. These data suggested stronger winds near its CSC and supported its determination as a WTD.

06 UTC, 28 July (Figure 4.3, Figure 4.4 (b))

At 06 UTC on 28 July, the OCCS was diagnosed as T1.5 because its cyclonic circulation became more evident from satellite imagery. This result meant that the system was highly likely to be determined as a WTD and also had a high possibility of developing to a TS. In this case, it was determined as an ExpT in ASAS because NWP clearly indicated its development within 24 hours. QuikSCAT data without rain flags at 09 UTC the same day indicated that it had a definite cyclonic circulation and winds of over 30 kt near its CSC.

[5] An LPA is a TC without definite cyclonic surface wind circulation where surface air pressures are lower than those of the surroundings.

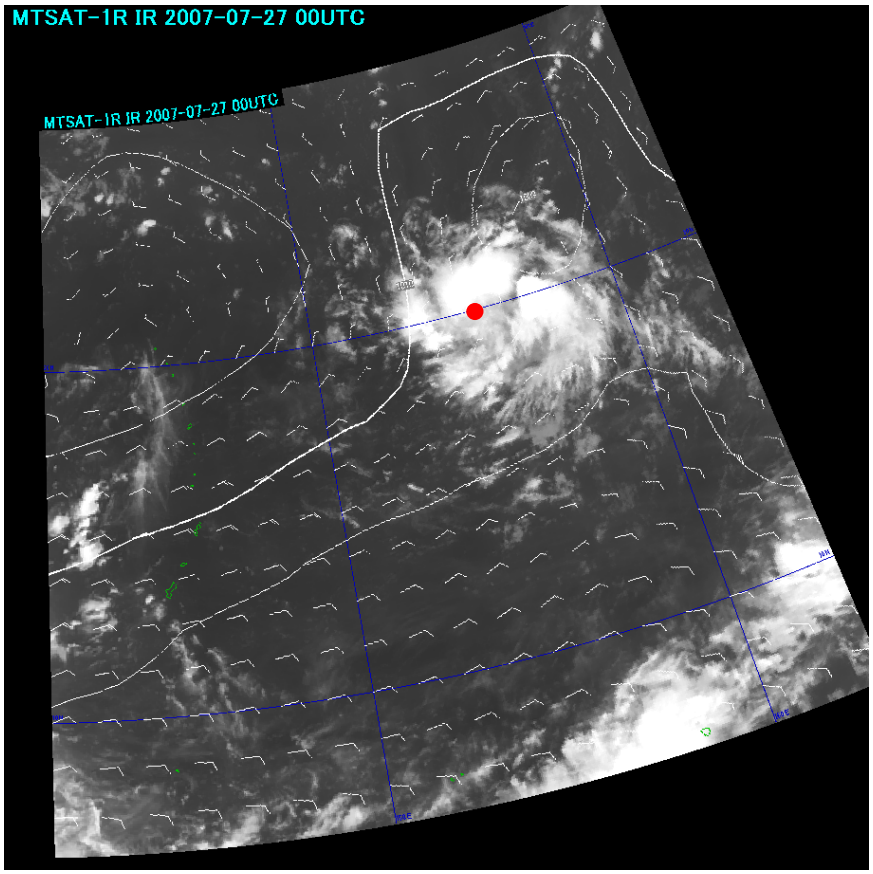

(a) Satellite image
The white arrows and lines and the red dot indicate NWP's surface winds, surface isobars and the CSC position of the OCCS respectively.

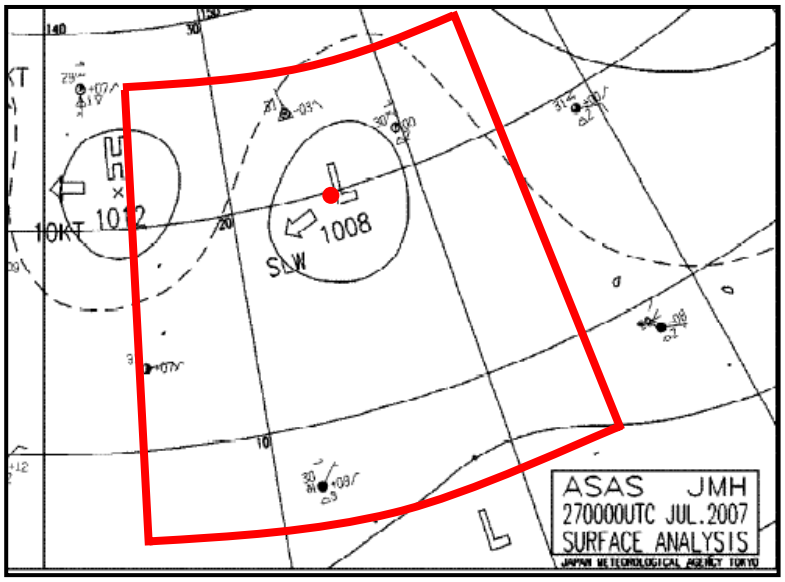

(b) Surface Analysis
The red dot indicates the CSC position of the OCCS. The area surrounded by the red line shows the coverage area of the above satellite image.

Figure 4.1 Satellite image and surface analysis for 00 UTC on 27 July 2007

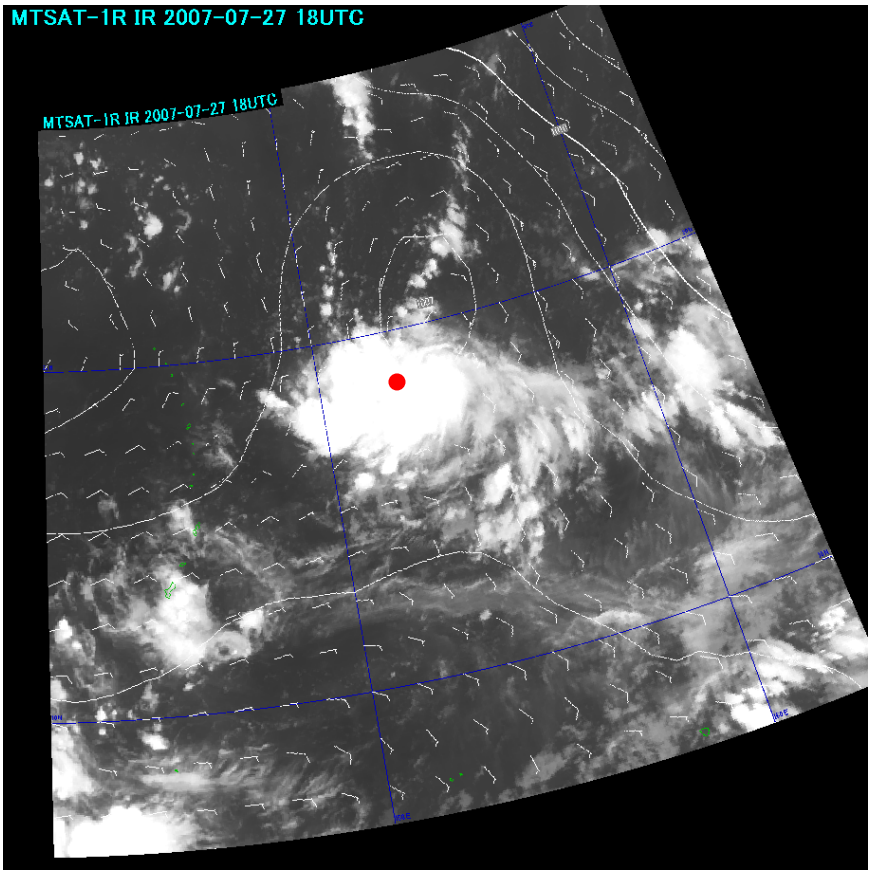

(a) Satellite image

The white arrows and lines and the red dot indicate NWP's surface winds, surface isobars and the CSC position of the OCCS respectively.

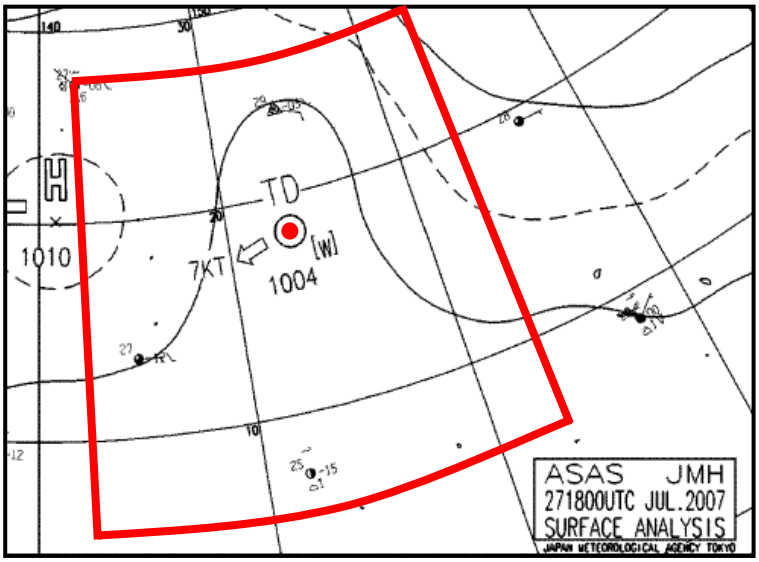

(b) Surface Analysis

The red dot indicates the CSC position of the OCCS. The area surrounded by the red line shows the coverage area of the above satellite image.

Figure 4.2 As Figure 4.1, but for 18 UTC on 27 July 2007

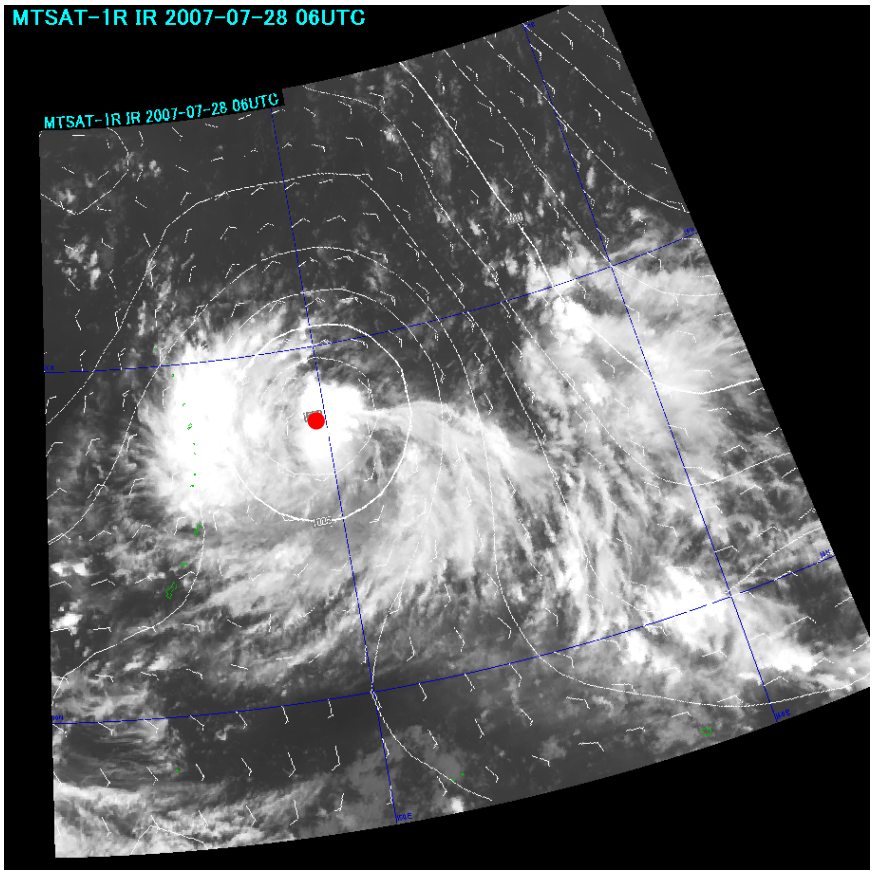

(a) Satellite image

The white arrows and lines and the red circle indicate NWP's surface winds, surface isobars and the CSC position of the OCCS respectively.

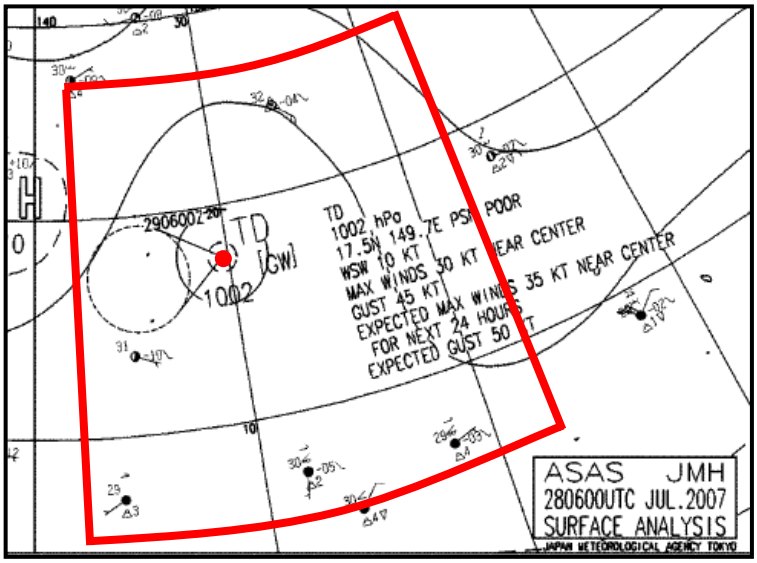

(b) Surface Analysis

The red indicates the CSC position of the OCCS. The area surrounded by the red line shows the coverage area of the above satellite image.

Figure 4.3 As figure 4.1, but for 06 UTC on 28 July 2007

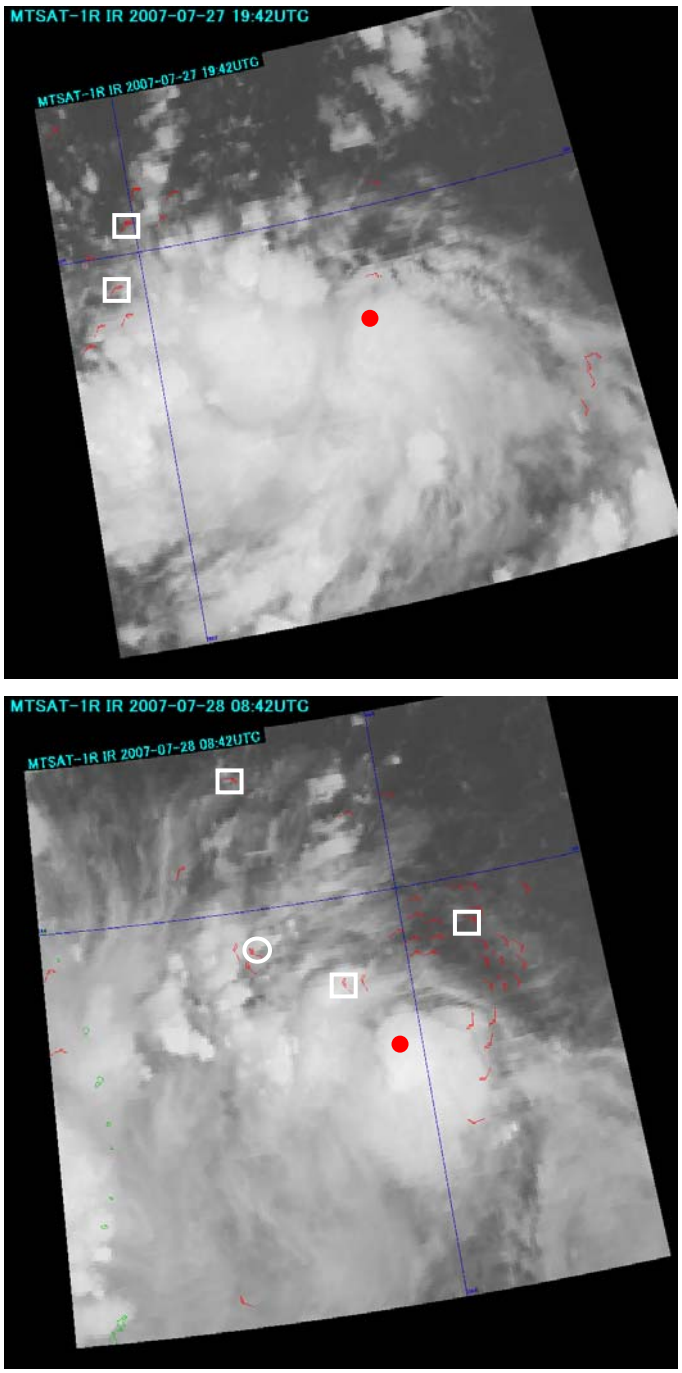

Figure 4.4 Satellite image and QuikSCAT winds of over 20 kt without rain flags (red arrows) at 20 UTC on 27 July (upper) and 09 UTC on 28 July (lower)

Each red dot indicates the CSC position at 18 UTC on 26 July (upper) and 06 UTC on 27 July (lower). Red arrows within circles and squares indicate winds of 25 to 30 kt and 30 to 35 kt respectively.

5. Conclusion

The revised EDA is one of the most important tools JMA uses to analyze TCs in the early developing stage. Table 5.1 shows typical examples of TC analysis in the early developing stage. Both Dvorak analysis and EDA are subjective methods, and their results depend on the operators involved. For this reason, their objectivization remains an issue to be solved.

Table 5.1 Typical examples of TC analysis in the early developing stage using surface observation data, QuikSCAT data, satellite imagery and NWP data, depending on the T-number of the OCCS.

<table>
<tr><th>T-number</th><th>Determination as TD</th><th>Determination as WTD</th><th>Determination as ExpT</th></tr>
<tr><td>0.0</td><td>It is monitored as a potential TD.</td><td rowspan="2">It is monitored as a potential WTD.</td><td rowspan="2">It is monitored as a potential ExpT.</td></tr>
<tr><td>0.5</td><td>If it has definite cyclonic wind circulation and winds of near Beaufort Force 6 or more, it is determined as a TD.</td></tr>
<tr><td>1.0</td><td rowspan="3">It is determined as a TD.</td><td>If it has winds of near Beaufort Force 7 or more, it is determined as a WTD.</td><td>If it has winds of near Beaufort Force 7 or more and NWP predicts the definite development within 24 hours, it is determined as an ExpT.</td></tr>
<tr><td>1.5</td><td rowspan="2">It is determined as a WTD.</td><td>If NWP predicts the development within 24 hours, it is determined as an ExpT.</td></tr>
<tr><td>2.0</td><td>It is determined as an ExpT.</td></tr>
</table>

References

Dvorak, V.F. (1984): Tropical Cyclone Intensity Analysis Using Satellite Data, NOAA Technical Report NESDIS 11, U.S. Dept. of Commerce.

K. Kishimoto, T. Nishigaki, S. Nishimura and Y. Terasaka (2007): Comparative Study on Organized Convective Cloud Systems detected through Early Stage Dvorak Analysis and Tropical Cyclones in Early Developing Stage in the Western North Pacific and the South China Sea, RSMC Tokyo – Typhoon Center Technical Review No.9, 19-32.

A. Tsuchiya, T. Mikawa and A. Kikuchi (2000): Discriminating method of cloud systems which develop into tropical cyclone in the early stage, Meteorological Satellite Center Technical

Note No. 38, 13-19 (in Japanese).

Tsuchiya, A., Mikawa, T. and Kikuchi, A. (2001): Method of Distinguishing Between Early Stage Cloud Systems that Develop into Tropical Storms and Ones that Do Not, Geophysical Magazine Series 2, Vol.4, Nos.1-4, 49-59.

The Possibility of Determining Whether Organized Cloud Clusters Will Develop into Tropical Storms by Detecting Warm Core Structures from Advanced Microwave Sounding Unit Observations

Kotaro Bessho
Typhoon Research Department, Meteorological Research Institute,
Nagamine 1-1, Tsukuba 305-0052, Japan

Tetsuo Nakazawa,
Typhoon Research Department, Meteorological Research Institute,
Nagamine 1-1, Tsukuba 305-0052, Japan

Shuji Nishimura
Japan Meteorological Agency / Regional Specialized Meteorological Center Tokyo – Typhoon Center
1-3-4 Otemachi, Chiyoda-ku, Tokyo, Japan

Koji Kato
Japan Meteorological Agency / Meteorological Satellite Center
3-235 Nakakiyoto, Kiyose-shi, Tokyo, Japan

Abstract

The air temperature profiles of organized cloud clusters developing or not developing into tropical storms (TSs) over the western North Pacific in 2004 were investigated from Advanced Microwave Sounding Unit (AMSU) observations and the results of Dvorak analyses for the cloud clusters. First, typical temperature profiles of the clusters developing or not developing into TSs were compared. From this comparison, positive temperature anomalies in the upper troposphere were found in both clusters, while the values and spatial sizes of the anomalies for the clusters that developed into TS were larger than those for the ones that did not. Statistical analysis was then performed on the temperature anomalies near the center of all clusters retrieved from AMSU observational data. The average anomalies increased along with the intensity of the clusters indicated by the T-number, as estimated using the Dvorak technique. Time series analysis of temperature anomalies in the upper levels of the clusters was performed, and warm core structures were defined by the threshold derived from these anomalies. Using this definition, almost 70% of the clusters that had warm cores developed into TSs, while 85% of those that did not finally dissipated without such development. For the warm-core clusters that developed into TSs, the lead time from the detection of their warm core using AMSU observations to their recognition as TS was 27.7 hours. It is suggested that there is a strong possibility of detecting and forecasting the genesis of TSs using air temperature anomalies derived from AMSU data.

1. Introduction

Many cloud clusters form over the western North Pacific. Some of these are well organized, rotate cyclonically, and finally develop into tropical storms (TSs), although most dissipate without such development. Despite the importance of distinguishing whether clusters will turn into TSs in terms of marine warnings and tropical cyclone forecasting, it remains difficult to forecast tropical cyclone genesis using numerical models. For this reason, forecasters at tropical cyclone warning centers worldwide have relied operationally on the Dvorak technique to estimate the potential of clusters to develop into TSs (Dvorak 1975 and Dvorak 1984). This technique is based on subjective analysis, and is used as a tool for judging the formation of tropical cyclones and evaluating their intensity from values such as the central surface pressure and maximum wind speed using the patterns and features of clouds observed by visible and infrared imagers on satellites. The *Tropical number* (T-number) index is defined in the Dvorak technique to express the intensity of a tropical cyclone. T-numbers range from one to eight, and are counted in increments of 0.5. T-number 1 (T1) corresponds to the minimum level of tropical cyclone intensity, while T8 describes the maximum level.

The Dvorak technique has endured for more than 30 years, and has saved huge number of lives from tropical cyclones (Velden *et al*. 2006). While this technique is considered to be a de facto standard of satellite analysis for tropical cyclones, it is not without its limitations. First, it involves subjective analysis, and considerable training and experience are needed to master the technique. Second, it is difficult to estimate the intensity of tropical cyclones correctly in their genesis stage, especially when central dense overcasts cover the cyclonic circulation at low level. Tropical cyclones in the genesis stage are usually so small that they cannot be analyzed properly using the Dvorak method, especially when dealing with tropical cyclones formed from monsoon troughs in the western North Pacific. While an objective version of the Dvorak technique has been developed to overcome the first limitation (Velden *et al*. 1998), there is a strong need for a new approach to break the barriers represented by the genesis stage of tropical cyclones.

Recently, microwave sensors on board low-earth-orbit satellites have been significantly improved and enhanced, including microwave imagers, sounders and scatterometers. Among these, microwave imagers are used to fix the center of tropical cyclones and ascertain their structure (Hawkins *et al*. 2001 and Lee *et al*. 2002). They can detect microwave radiation from rain and ice particles through the dense clouds found in tropical cyclones. Using these characteristics of microwave imagers, Hoshino and Nakazawa (2007) presented an objective method of intensity estimation for tropical cyclones in the developing and mature stages. Microwave scatterometers can also estimate the sea surface wind distribution in and around tropical cyclones (Katsaros *et al*. 2001). By way of example, Sharp *et al*. (2002) and Gierach *et al*. (2007) inferred tropical cyclone genesis using the vorticity retrieved from observational data produced by the scatterometer of QuikSCAT. Unfortunately, however, occasions of QuikSCAT observation for one tropical cyclone are up to twice a day.

As a new generation of microwave sounders, Advanced Microwave Sounding Units (AMSUs) are now used to observe air temperature profiles within dense clouds at a more detailed level of spatial resolution than former sounders (Kidder *et al*. 2000). AMSUs are now employed on the NOAA-15, -16, -18 satellites, MetOp and the Earth Observing Satellite (EOS) Aqua. From the observations of five AMSUs, the air temperature structures of tropical cyclones can be sensed up to ten times a day. Moreover, warm core structures at the upper levels of tropical cyclones are retrieved from the temperature profiles observed by AMSUs. A warm core is defined as the center region of a tropical cyclone where the air temperature is higher than that of the surrounding environment because of the latent heat released by active convection within the cyclone. Warm cores are generally observed in the developing or mature stages of tropical cyclones (Hawkins and Rubsame 1968; Hawkins and Imbembo 1976; Heymsfield *et al*. 2001; Halverson *et al*. 2006). Though some research mainly targeting the developing or mature stages of tropical cyclones has statistically related the signals of warm cores detected by AMSU observations to the tropical cyclone intensity (Brueske and Velden 2003; Demuth *et al*. 2004; Demuth *et al*. 2006), the situation regarding warm core structures at the genesis stage of tropical cyclones remains unclear. This leaves the possibility of complementing the Dvorak technique to judge the genesis of tropical cyclones more objectively by using AMSU observations.

In this study, the air temperature structures of cloud clusters, some of which developed into TSs while others did not, were investigated using the AMSUs on board NOAA-15 and -16 in 2004. Particular attention was focused on the amplitude of positive temperature anomalies at 200 - 300 hPa in the clusters, as such anomalies correspond to warm cores. This article will first present the typical warm core structures of cloud clusters before investigating the amplitude of temperature anomalies at the upper levels of clusters classified by their final stage. The warm core structure in the cluster will then be defined using the threshold of the temperature anomalies. Finally, from the statistical analysis results of the warm core structures in the clusters, we will discuss the possibility of distinguishing whether a cluster will develop into a tropical cyclone or not in terms of the existence of warm cores in the clusters.

2. Early stage Dvorak analysis

The Meteorological Satellite Center (MSC) of the Japan Meteorological Agency (JMA) routinely monitored Organized Cloud Clusters (OCCs) over the western North Pacific that had the potential to develop into TSs (defined in terms of Tsuchiya *et al.* (2001)), and logged their locations and T-numbers since 1999 at six-hourly intervals. This process is called early stage Dvorak analysis (EDA). EDA is a part of JMA's Dvorak analysis, and also depends on subjective judgment using observational data from geostationary satellites. We used data from the results of EDA in this study to classify OCCs by their final stage.

JMA classifies tropical cyclones over the western North Pacific ocean into four grades based on their maximum wind speed (MWS) as shown in Table 1; they are typhoon (TY, MWS of 64 kt or more), severe tropical storm (STS, MWS of 48 kt or more and less than 64 kt), tropical storm (TS, MWS of 34 kt or more and less than 48 kt), and tropical depression (TD, MWS of 34 kt or less). JMA also names tropical cyclones with a MWS of 34 kt or more and issues gale warnings for them to marine users. EDA, which is employed to distinguish TDs from TSs, includes the two steps outlined below.

Table 1 Classification of tropical cyclones by JMA

Type of Tropical Cyclones	Maximum Wind Speed (MWS)	Code
Low Pressure Area		L
Tropical Depression	34 kt > MWS	TD
Tropical Storm	48 kt > MWS ≥ 34 kt	TS
Severe Tropical Storm	64 kt > MWS ≥ 48 kt	STS
Typhoon	MWS ≥ 64 kt	T

As the first step, analysts investigate the cloud cluster's Cloud System Center (CSC) to distinguish OCCs from other cloud clusters. In this paper, an OCC is defined as a cloud cluster with a CSC. According to Dvorak (1984), a CSC has at least one of the four features below (illustrated in Figure 1). To determine the CSC, analysts select the most suitable one of the following:

i) Dense, cold (-31 ^{o}C or colder) overcast bands that show some curvature around a relatively warm area. They should curve at least one-fifth of the distance around a ten-degree logarithmic spiral. When visible observations are available, cirrus lines will indicate anticyclone shear across the expected CSC.

ii) Curved cirrus lines indicating a center of curvature within or near a dense, cold (-31 ^{o}C or colder) overcast.

iii) Curved low cloud lines showing a center of curvature within two degrees of a cold (-31 ^{o}C or colder) cloud mass.

iv) Cumulonimbus (Cb) clusters rotating cyclonically in animated images.

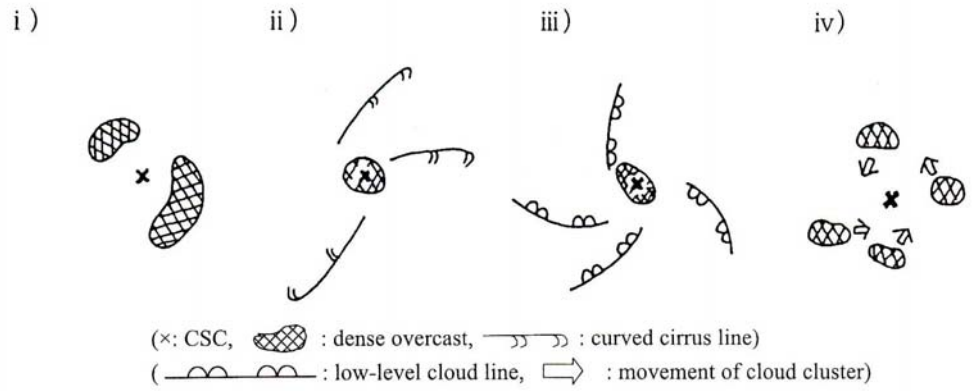

Figure 1 CSCs defined from four cloud patterns (i-iv) (after Tsuchiya *et al.* (2001))

After detecting the CSC, analysts give a T-number 1 (T1) diagnosis and judge the cyclogenesis as the second step of EDA. In this diagnosis, the T-number is determined as 1 when cloud systems have all five of the following conditions (Figure 2):

(1) The cloud clusters have persisted for 12 hours or more.

(2) The accuracy of estimation for the CSC in the clusters is 2.5° latitude or less.

(3) The CSC has persisted for six hours or more.

(4) The clusters have dense, cold (-31 °C or colder) overcasts that appear less than 2° latitude from the CSC.

(5) The extent of the overcasts is more than 1.5° latitude.

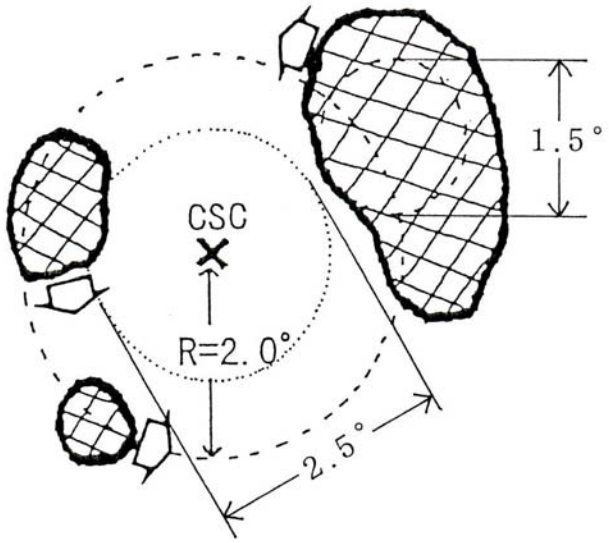

Figure 2 A conceptual model of cloud clusters satisfying T1. The shaded areas are dense, cold (-31 °C or colder) overcasts. The estimation accuracy of the CSC is expressed by the dotted circle around it with a diameter of 2.5° (2). The broken circle with a radius of 2.0° indicates the region including the dense, cold overcast (4). The diameter of the circle drawn in the overcast on the right side of the CSC is 1.5°. This circle shows the size of the overcast (5). (after Tsuchiya *et al.* (2001))

An OCC is usually identified as a TD (not yet a TS) when the T-number becomes 1 or more, and is judged as a TS when the MWS of the TD reaches 34 kt or more. On the other hand, an OCC with a T-number smaller than 1 is referred to as a low-pressure area (L) in EDA.

In this study, OCCs are classified by their final stage as follows: OCC_L are OCCs that stayed at the stage of L and finally dissipated; OCC_{TD} are OCCs that developed into TDs, but did not develop into TSs; OCC_{TS} are OCCs that developed into TSs.

3. Data

AMSU brightness temperature data from NOAA-15 and -16 in 2004 came courtesy of the Cooperative Institute for Research in the Atmosphere (CIRA) of Colorado State University (CSU). The air temperature profiles around OCCs were retrieved by a DDK algorithm developed by CIRA (Demuth *et al.* 2004 and Bessho *et al.* 2006). The retrieved temperature data on the footprint of AMSU were interpolated into a grid of 24° latitude by 24° longitude with a resolution of 0.2° centered on the CSC of OCCs after Barnes (1964). The retrieved air temperature data set had 30 pressure levels from 1000 to 10 hPa.

Air temperature anomalies were used for analysis of the warm core structure in OCCs. To calculate the temperature anomalies, the mean air temperature in a rectangular frame of 10° latitude by 10° longitude centered on the CSC of OCCs was subtracted from the air temperature at

each pressure level, which is almost the same as the method used by Knaff *et al*. (2004).

The EDA log file for 2004 lists 100 OCCs in the western North Pacific. Among them, 29 were $OCC_{TS,}$ 14 were OCC_{TD}, and the others were OCC_L. Eliminating the six cases with no AMSU observational data, 28 cases of OCC_{TS}, 13 cases of OCC_{TD} and 53 cases of OCC_L were used in this study. As the number of OCC_{TD} is too small to compare with those of OCC_L or OCC_{TS}, this study will mainly show the results of comparison between OCC_L and OCC_{TS}.

4. Examples of warm core structures of OCCs estimated from AMSU

The typical warm core structures of two OCCs are shown here before presenting the statistics of the air temperature anomalies retrieved from AMSU within OCCs. One OCC is numbered as 0428 (referred to below as EDA0428), and the other is as 0453 (EDA0453). EDA0428, which was an OCC_L, was detected as an OCC at 18Z on 3 June 2004 at 8.2° N and 151.4° E, and dissipated at 06Z on 4 June after a lifetime of just 12 hours. On the other hand, EDA0453, an OCC_{TS}, was first detected as an OCC at 06Z on 13 August 2004 at 13.2° N and 144.4° E. It reached T-number 1 at 00Z on 14 August at 14.5° N and 140.5° E and became a TD. It finally developed into a TS at 06Z on 16 August at 18.8° N and 130.8° E, and was named Typhoon Megi. JMA numbered this typhoon 0415.

Figure 3 shows Geostationary Operational Environmental Satellite-9 (GOES-9) infrared imagery and AMSU air temperature anomalies at the level of 200 hPa for EDA0428 at 21Z on 3 June and EDA0453 at 21Z on 13 August. At 21Z on 3 June, three hours had passed since EDA0428's genesis, whereas 15 hours had passed at 21Z on 13 August since EDA0453's detection as an OCC. It took two-and-a-half days to reach the stage of TS. While EDA0453 had very large and active convective clouds near its CSC, EDA0428 had scattered convective clouds near the center. Though both OCCs have positive temperature anomalies in the AMSU observational images, they look quite different. For EDA0453 of OCC_{TS}, the area of positive anomalies spreads widely corresponding to the large convective areas around its CSC, and the maximum temperature

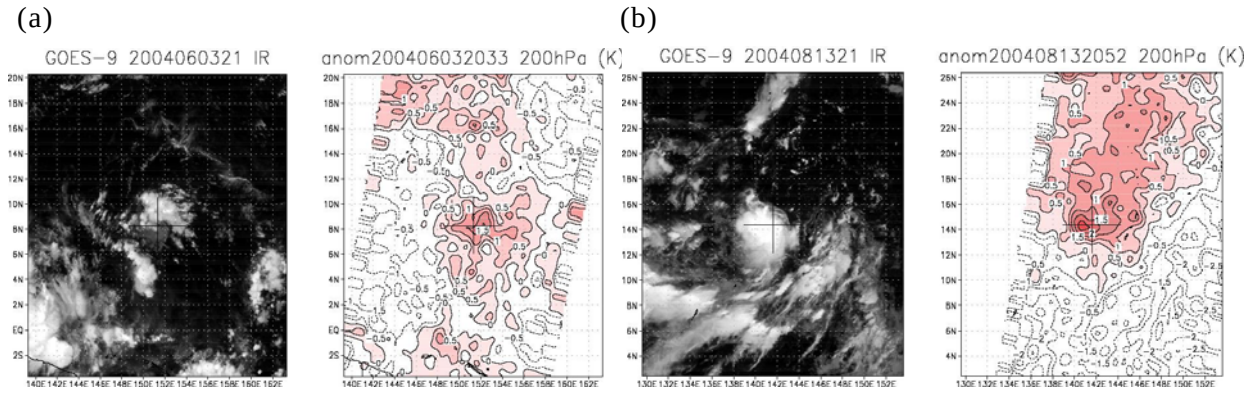

Figure 3 Horizontal images of AMSU-retrieved temperature anomalies (K) at 200 hPa (right) and GOES-9 infrared brightness temperatures (left) for (a) EDA0428 at 21Z on 3 June, and (b) EDA0453 at 21Z on 13 August. The cross hairs in the images show the position of the CSC.

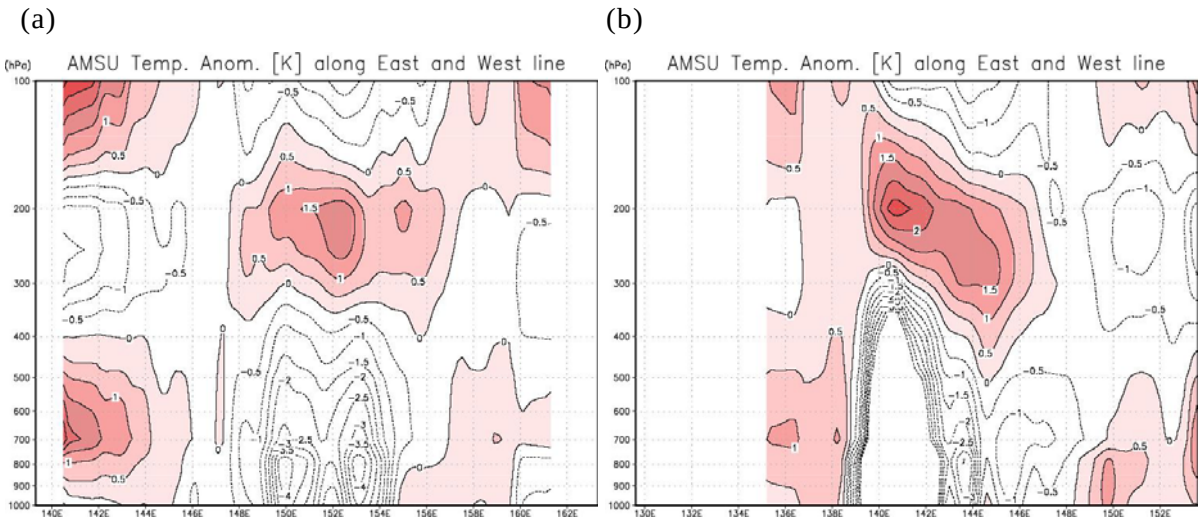

Figure 4 Vertical cross sections of AMSU-retrieved temperature anomalies (K) along an east-to-west line through the CSC at the same observational time as Figure 3 for (a) EDA0428 and (b) EDA0453.

anomaly reached 2.5 K or more. In contrast, EDA0428 of OCC_L shows small regions of positive temperature anomalies and a maximum value of 1.5 K.

Figure 4 shows vertical cross sections of the air temperature anomalies in OCCs retrieved from AMSU data along an east-to-west line through the CSC at the same observational time as Figure 3. Note that retrieved air temperatures are not reliable near the center of OCCs below 300 hPa because of contamination from heavy rainfall. Both EDA0428 and EDA0453 have positive temperature anomalies near the center from 300 hPa to 150 hPa. While the peak temperature anomaly for EDA0428 is 1.5 K and is located at 250 - 200 hPa over the CSC, the peak for EDA0453 is 2.5 K or more, and is located at 200 hPa.

Figure 5 shows the pressure-time cross sections of air temperature anomalies of OCCs

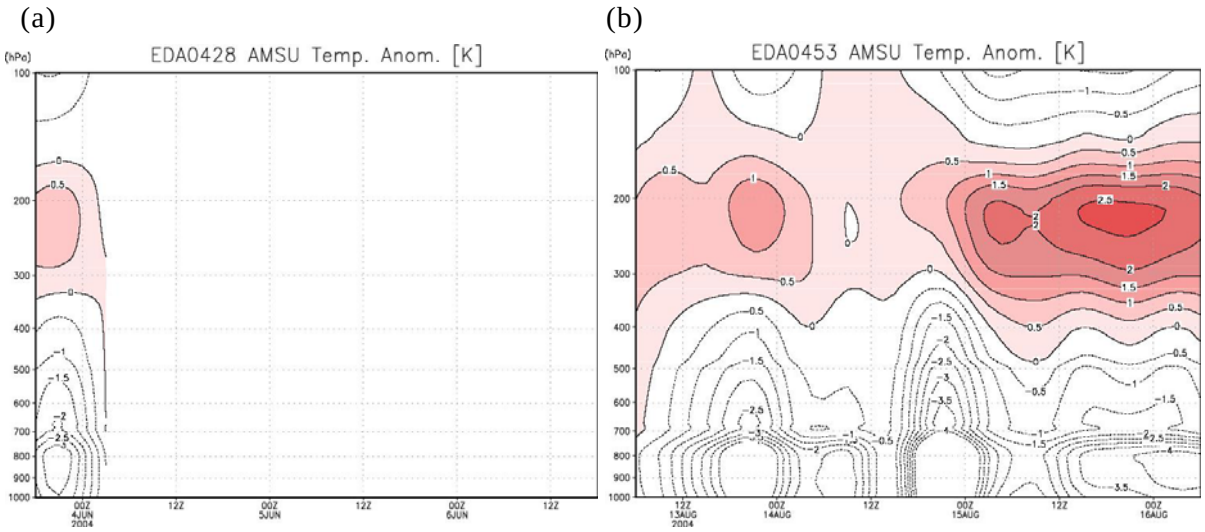

Figure 5 Pressure-time cross sections of air temperature anomalies (K) averaged within a rectangle of 4° latitude by 4° longitude centered on the CSCs retrieved from AMSU observations in the cases of (a) EDA0428 and (b) EDA0453.

Table 2 Statistics of air temperature anomalies retrieved from AMSU within OCCs classified by their final stage and T-number at (a) 200 hPa, (b) 250 hPa and (c) 300 hPa. Statistically significant values at the 95% level are denoted by an asterisk.

(a)

200 hPa	Number of cases	T-number	Avg. anom. in 4^o x 4^o	Max. anom. in 10^o x 10^o	Fraction of anomalies more than 1 K in 4^o x 4^o
OCC_L	108	0.0	0.11 (0.48)*	2.06 (0.73)*	10.6 (16.0)*
OCC_{TD}	47	0.0	0.37 (0.50)	2.25 (0.70)*	18.7 (19.0)
	36	1.0	0.26 (0.45)	2.25 (0.76)*	14.0 (17.9)
	11	1.5	0.66 (0.71)	2.53 (1.24)	27.9 (27.0)
OCC_{TS}	76	0.0	0.39 (0.54)	2.22 (0.66)*	20.4 (21.5)
	76	1.0	0.56 (0.59)*	2.19 (0.75)*	28.3 (26.9)*
	29	1.5	0.72 (0.70)*	2.47 (0.80)*	36.1 (30.2)*
	28	2.0	0.93 (0.63)*	2.51 (0.87)*	42.9 (31.4)*

(b)

250 hPa	Number of cases	T-number	Avg. anom. in 4^o x 4^o	Max. anom. in 10^o x 10^o	Fraction of anomalies more than 1 K in 4^o x 4^o
OCC_L	108	0.0	0.05 (0.41)*	1.47 (0.47)*	3.9 (9.1)*
OCC_{TD}	47	0.0	0.31 (0.47)	1.54 (0.40)*	12.1 (19.0)
	36	1.0	0.28 (0.41)	1.70 (0.41)*	10.8 (16.4)
	11	1.5	0.59 (0.54)	1.71 (0.59)	22.3 (29.5)
OCC_{TS}	76	0.0	0.40 (0.48)	1.60 (0.43)*	17.3 (24.0)
	76	1.0	0.51 (0.53)*	1.54 (0.51)*	20.8 (26.9)
	29	1.5	0.67 (0.65)*	1.72 (0.67)*	30.3 (34.3)*
	28	2.0	0.76 (0.58)*	1.74 (0.65)*	35.2 (34.4)*

(c)

300 hPa	Number of cases	T-number	Avg. anom. in 4^o x 4^o	Max. anom. in 10^o x 10^o	Fraction of anomalies more than 1 K in 4^o x 4^o
OCC_L	108	0.0	-0.02 (0.44)*	1.15 (0.45)*	2.4 (9.5)*
OCC_{TD}	47	0.0	0.15 (0.51)	1.28 (0.40)*	8.0 (18.2)
	36	1.0	0.23 (0.49)	1.39 (0.43)*	12.0 (23.9)
	11	1.5	0.37 (0.48)	1.43 (0.44)	20.2 (25.1)
OCC_{TS}	76	0.0	0.31 (0.44)	1.28 (0.41)*	10.8 (17.3)
	76	1.0	0.32 (0.48)	1.27 (0.43)*	11.8 (20.6)
	29	1.5	0.43 (0.62)*	1.37 (0.47)*	19.5 (26.9)*
	28	2.0	0.40 (0.65)	1.50 (0.54)	24.8 (27.1)*

average within a rectangle of 4^o latitude by 4^o longitude centered on the CSC. Though EDA0428 has positive anomalies between 300-200 hPa, the values were less than 1 K around 21Z on 3 June when the horizontal and vertical snapshots in Figures 3(a) and 4(a) were observed. On the other hand, the anomalies of EDA0453 are sometimes large and sometimes small. At 21Z on 13 August (the same time as Figures 3(b) and 4(b)), the anomalies peaked at more than 1 K before becoming weaker and then breaking the 1 K level again. From 12Z on 15 August, EDA0453 had anomalies of more than 2 K.

5. Statistics of air temperature anomalies at upper levels for each OCC case

In this section, the statistics of air temperature anomalies at 200 - 300 hPa for OCCs are

presented as Table 2, and are classified by their final stage and T-number. At 200 hPa, the temperature anomalies of OCC_{TS} averaged within a rectangle of 4^o latitude by 4^o longitude centered on the CSC increase along with their T-number (Table 2 (a)). When the T-number is 0.0, the average anomaly is 0.39 K. The anomaly shows a value of 0.56 K with a T-number of 1.0 at which OCCs reach the TD stage, and shows 0.72 K for a T-number of 1.5. The average temperature anomaly finally reached 0.93 K with a T-number of 2.0 and larger (corresponding to the stage of TS), which is more than twice the value at a T-number of 0.0. This increasing tendency of average temperature anomalies at 200 hPa near the center of OCCs with T-numbers is similar to those at 250 and 300 hPa (Table 2 (b) and (c)).

On the other hand, average maximums of air temperature anomalies at 200 hPa of OCC_{TS} within a rectangle of 10^o latitude by 10^o longitude centered on the CSC show almost constant values of 2.2 - 2.5 K, and average maximums of anomalies at 250 and 300 hPa of OCC_{TS} also have almost constant values of 1.5 - 1.7 K and 1.3 - 1.5 K respectively, which are smaller than the value at 200 hPa. Considering the percentages of grid numbers for air temperature anomalies of more than 1 K within a rectangle of 4^o latitude by 4^o longitude centered on the CSC at 200 hPa of OCC_{TS}, the fractions of the air temperatures increase from 20.4% with a T-number of 0.0 to 42.9% with a T-number of 2.0. This tendency is also found from the percentages of grid numbers at 250 and 300 hPa.

In Table 2, some values are statistically significant at the 95% level, while others are not. From these tables, however, it is roughly understood that average temperature anomalies and the percentages of grid numbers of temperature anomalies more than 1 K near the center of the OCCs demonstrate an upward trend along with their T-numbers. This means that most OCCs have positive temperature anomalies called *warm cores* at troposphere upper levels. It is also understood that OCCs with larger T-numbers usually have larger temperature anomaly values than those with smaller T-numbers. If OCCs have the same T-number of 0.0, the average OCC_{TS} temperature anomalies are larger than those of OCC_L. In contrast, the average maximum air temperature anomalies of OCCs have almost constant values for all T-numbers.

6. Time series of air temperature anomalies at upper levels for each OCC case

Time series graphs of the temperature anomalies at upper levels were drawn for each OCC case. The objective was to understand the tendency of air temperature anomalies calculated from AMSU data and to find the threshold value of the anomalies to distinguish OCCs that developed into TSs from those that did not.

Figure 6(a) shows a time series of the air temperature anomalies at 200 hPa averaged within a rectangle of 4^o latitude by 4^o longitude centered on the CSC for all cases of OCC_L. For all cases except one, all lines are located below 0.9 K, and at 200, 250 and 300 hPa, only three cases of OCC_L have temperature anomalies of more than 0.9 K in their lifetime. This means that the temperature anomalies did not reach 0.9 K in the other 50 OCC_L cases. Figures 6(b) and (c) show

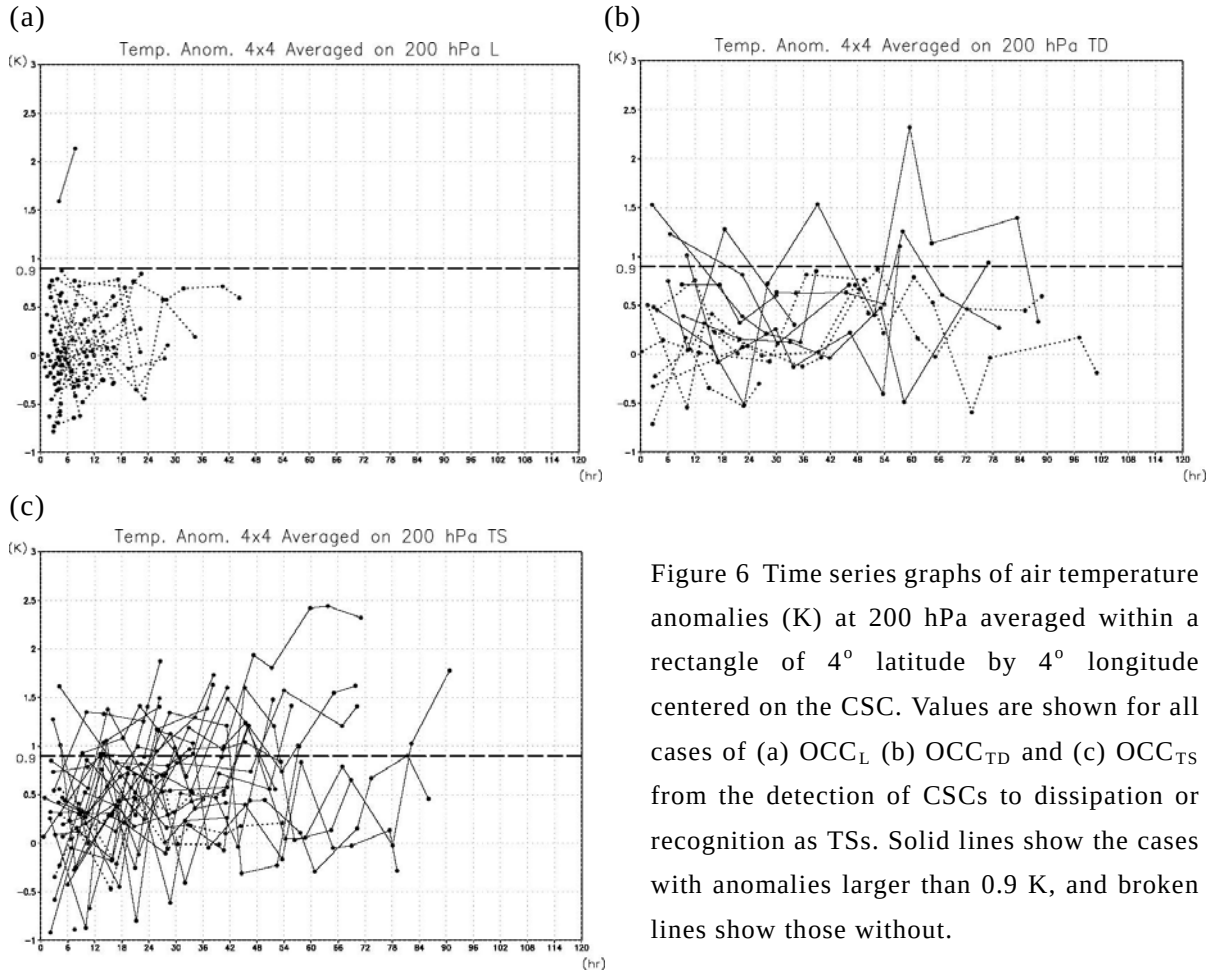

Figure 6 Time series graphs of air temperature anomalies (K) at 200 hPa averaged within a rectangle of 4^o latitude by 4^o longitude centered on the CSC. Values are shown for all cases of (a) OCC_L (b) OCC_{TD} and (c) OCC_{TS} from the detection of CSCs to dissipation or recognition as TSs. Solid lines show the cases with anomalies larger than 0.9 K, and broken lines show those without.

similar time series graphs of the temperature anomalies at 200 hPa for all cases of OCC_{TD} and OCC_{TS}. In most cases of OCC_{TS}, temperature anomalies become larger than 0.9 K at least once in their lifetime. For the cases of OCC_{TD}, almost half have anomalies larger than 0.9 K. From these observation results, we can conclude in this study that OCCs have a warm core structure at their upper levels when their air temperature anomalies (averaged within a rectangle of 4^o latitude by 4^o longitude centered on the CSC) exceed 0.9 K at 200, 250 or 300 hPa on one or more occasions in their lifetime.

Table 3 shows the number of OCCs classified by this definition, indicating that a total of 25 of 28 OCC_{TS} have warm core structures. On the other hand, 50 out of 53 OCC_L do not have a warm core. It is revealed that 89% of OCC_{TS} have a warm core at least once in their lifetime, while 94% of OCC_L do not. It is also clear that while almost 70% of all OCCs with a warm core structure developed to TS level, 85% of those with

Table 3 Numbers of each kind of OCC with or without warm core (WC) structures.

	With WC	Without WC	Total
OCC_L	3	50	53
OCC_{TD}	7	6	13
OCC_{TS}	25	3	28

no warm core stayed at the stage of L and dissipated. The threshold of 0.9 K as the definition of a warm core in the time series of upper temperature anomalies of OCCs is expected to be useful in distinguishing whether an OCC will develop into a TS.

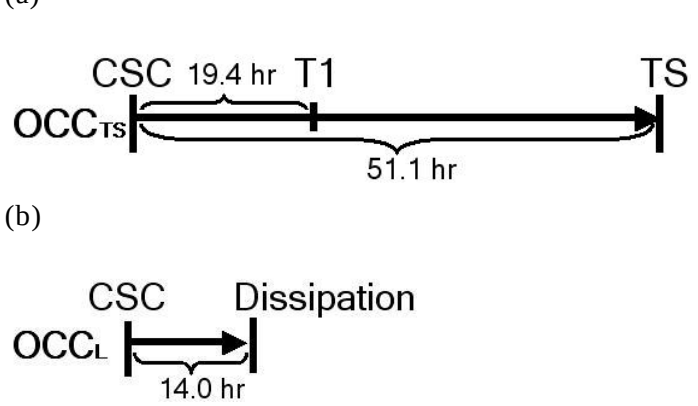

Figure 7 Schematic diagram of the average lifetime of (a) 25 cases of OCC_{TS} with a warm core and (b) 50 cases of OCC_L with no warm core. In the diagram, 'CSC' means the detection of the CSC, 'T1' represents the first judgment as T1, and 'TS' refers to the evolution of TS status.

7. Duration from detection of CSC to each stage in OCCs

For 25 cases of OCC_{TS} with a warm core, the average time from the detection of the CSC to evolution into a TS was 51.1 hours in 2004 (Figure 7(a)). This means that the OCC_{TS} takes approximately two days to become a TS from the status of low-pressure area, and an average of 19.4 hours to reach the stage of T-number 1 (T1) for the first time from its appearance as an OCC. Meanwhile, the durations of 50 cases of OCC_L with no warm core from detection as an OCC to dissipation averaged only 14.0 hours (Figure 7(b)), which indicates that an OCC_L with no warm core structure usually dissipates in around half a day.

On the other hand, for OCC_{TS} with a warm core, the average time from detection as an OCC to the first recognition of their warm core structures in AMSU observations is 23.4 hours (Figure 8). This duration almost corresponds to the period from the appearance of an OCC to the first judgment of T1. For two cases of OCC_L with a warm core structure, the average time from detection as an OCC to the first recognition of a warm core structure was only 3.7 hours, and the average lifetime was 8 hours.

8. Discussion

Most previous studies on the structure and environmental field of tropical cyclones in the genesis stage in the western North Pacific have handled only cases of cloud clusters that developed to TS status (Briegel and Frank 1997; Ritchie and Holland 1999; Dickinson and Molinari 2002; Cheung 2004). This is because there was no official record for those that did not develop into TSs. Although such studies found important characteristics in the formation of tropical cyclones, most of these were *necessary conditions*. To reveal *sufficient conditions*, cloud clusters

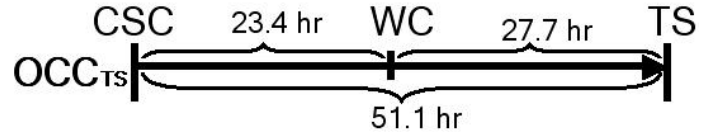

Figure 8 Schematic diagram of the average lifetime of 25 cases of OCC_{TS} with a warm core. In the diagram, the abbreviations are the same except for 'WC', which represents the first recognition of a warm core from AMSU observation.

that did not develop into TSs must be analyzed. Exceptions to these previous studies include works by CSU researchers published in the 1980s and 1990s (McBride and Zehr 1981; Lee 1989; Zehr 1992). In these papers, the authors used data obtained from soundings (McBride and Zehr 1981; Lee 1989), objective analysis (Zehr 1992) and satellite infrared imagery (Zehr 1992), and picked up many clusters that developed or did not develop into TSs in the western North Pacific. Our study also treats these clusters classified using EDA by MSC operationally. These EDA results include not only clusters with an intensity larger than that of TDs, but also tiny clusters at the start of rotation, which is a distinctive feature of our study. The analyses in this study were carried out using AMSU data representing the newest microwave sounding observations from low-earth-orbit satellites, which can detect warm core structures in cloud clusters directly. This is another advantage of the present paper compared with the earlier studies by CSU using the data of soundings, objective analyses and infrared imagery.

From Table 2, it was found that the average air temperature anomalies at the upper levels near the center of OCC_{TS} increase along with their T-numbers. On the other hand, the average maximum air temperature anomalies at the upper levels of OCC_{TS} keep almost constant values. The value at one grid point represents the air temperature within a rectangle of 0.2^{o} latitude by 0.2^{o} longitude in which there may be clear sky or many kinds of clouds, and the maximum air temperature anomaly of each OCC_{TS} is the value of one grid point extracted from all grid points in an observational area. It is clear that the average maximum temperature anomaly for all T-numbers has an almost constant value because the total amount of latent heat released from each convective cloud system included in one grid point has an upper limit. Meanwhile, the average temperature anomalies near the center of OCCs become larger with increased T-numbers. This phenomenon depends on the enlargement of the convective area within OCCs accompanying the increase of T-numbers. This is also understandable from the variation of fractions of temperature anomalies of more than 1 K near CSC of OCCs.

The percentage of grid points with anomalies of more than 1 K at 200 hPa of OCC_{L} with T-number of 0.0 is 10.6%. For OCC_{TS} with T-number of 0.0 at 200 hPa, the percentage is 20.4%, so it can be deduced that OCC_{TS} have double the convection area of OCC_{L}. Reflecting the difference between the percentages of grid points of anomalies more than 1 K in the two types of OCC, the average temperature anomalies of OCC_{TS} with T-number of 0.0 is 0.39 K, which is more than three times that of OCC_{L}. In EDA, OCCs need to satisfy the five conditions described in Section 2 to be diagnosed as T-number of 1.0. Both OCC_{L} and OCC_{TS} with T-number of 0.0 did not meet the requirements, but there is a distinct difference between their convective cloud system areas. It could be inferred that OCC_{TS} with T-number of 0.0 have some structural differences from OCC_{L} with T-number of 0.0. This presumption is another key to distinguishing OCC_{TS} from OCC_{L} at the stage of T-number of 0.0, but remains a future challenge.

The maximum temperature anomalies of OCC_{TS} with T-number of 1.0, which are significant at the 95% level, increase along with the height. The maximums are 1.27 K at 300 hPa,

1.54 K at 250 hPa, and 2.19 K at 200 hPa, and the same tendencies are also found from all classified OCC_S cases with T-numbers of 0.0 - 2.0. In previous observational studies, the heights of peak warm core anomalies vary from paper to paper, and differ from tropical cyclone to tropical cyclone. By way of example, the peak of the warm core in the intense Hurricane Hilda (1964) was located at 250 hPa (Hawkins and Rubsame 1968). On the other hand, the warming of Hurricane Erin (2001) was the greatest at 500 hPa (Halverson *et al*. 2006). In Knaff *et al*. (2004), it was found statistically that the peak of the warm core was located at the upper levels, and descended as the vertical wind shear increased for 186 tropical cyclone cases. They used air temperature information retrieved from AMSU brightness temperature data archived in CIRA, with a retrieval method same as that of this paper. The heights of warm core anomaly maximums are consistent between Knaff *et al*. (2004) and this paper because the same kinds of data set and retrieval method were used. However, there is a discrepancy between the height of the peak of 200 hPa in this paper (high) and that in other observational papers (low). The air temperatures at lower levels retrieved from AMSU data are cooler than normal, especially near the center of OCCs, due to the absorption and scattering of microwave radiation by liquid water and ice particles. This attenuation effect of microwaves could have brought lower maximum temperature anomalies at 300 hPa than those at 200 hPa.

In Zehr (1992), it was found that clusters developing into TSs have a stage of convective burst in their lifetime from genesis to emergence as a TS. Convective burst is a phenomenon of convection within clusters or tropical cyclones expressed by a peak of low infrared brightness temperature before appearance as a TSs. Once clusters experience convective burst, all the convections become active, and the phenomenon is usually found 24 hours before the incidence of tropical cyclones. In our study, temperature anomalies near the center of clusters at upper levels sometimes reach the peak before developing into tropical cyclones, as described in Figure 5(b). This appearance of a warm core structure within clusters at upper levels agrees with the convective burst in Zehr (1992). The convective burst is considered as the first occurrence of T-number 1 in EDA results, and has an average timing of 19.4 hours for the OCC_{TS} with a warm core in EDA files. The timing is almost the same as that of the first detection of a warm core in OCC_{TS} at an average of 23.4 hours. A possible scenario behind this is as follows: when the cluster has a convective burst in the infrared imagery, it is recognized as T-number 1. After a few hours, the convective burst provides large amounts of latent heat to the upper troposphere near the center of the cluster, and the warm core structure is observed by AMSU. This hypothesis must be proved by further studies.

As outlined in Chapter 7, the average period from the detection of the CSC of an OCC_{TS} to development into a TS is 51.1 hours (Figure 7(a)), and the period from the detection of the CSC in 25 cases of OCC_{TS} with warm cores to the first retrieval of the warm core is 23.4 hours (Figure 8). If the warm core retrieved from AMSU data is regarded as a sign of TS genesis, the lead-time to its genesis is 27.7 hours. This indicates that the detection of warm cores in OCCs is a very useful tool for finding and forecasting TS genesis.

On the other hand, there were three cases of OCC_{TS} in which no warm core structure was observed in the lifetime from detection of the CSC to evolution into TS, while three cases of OCC_{L} did have warm core structures. Among these OCC_{L} cases, one was a misdetection of a cold low as a tropical low in the EDA file. This phenomenon is the same as that reported by Knaff *et al*. (2000), who found that two cyclonic weather systems located in the South Pacific Ocean, despite their similar appearance in infrared imagery, had very different vertical thermal structures observed from AMSU. This study also confirmed that AMSU observation is useful in distinguishing cyclones with a warm core at upper levels from those with a cold core. Two of the three OCC_{TS} cases with no warm core structure did in fact have warm core structures located far from the lower vortexes. For OCC_{TD}, the total number of cases is small, but half of them had warm cores and half did not. These exceptions mean that 30% of OCCs with warm core structures did not develop into TSs, while 5% of OCCs with no warm core did develop to TS status. To improve the performance of determining whether OCCs will develop into TSs, it is necessary to add another screening method. One possible solution for this is to use the lifetime of the OCC from CSC detection to dissipation as L or to evolution into a TS. The average lifetime of an OCC_{L} with no warm core is 14.0 hours, and that of an OCC_{TS} is 51.1 hours. From the difference in these durations, it is expected that an OCC_{L} can be distinguished from an OCC_{TS} in conjunction with AMSU warm core detection.

From the above discussion, it can be concluded that there is a strong possibility of detecting and forecasting the formation of TSs from AMSU observations. However, it is still necessary to add more detailed analysis to develop an objective method of detecting and forecasting TS genesis by the retrieval of warm cores from AMSU data and the monitoring of OCC durations. EDA operation was transferred from MSC to the Regional Specialized Meteorological Center (RSMC) Tokyo - Typhoon Center operated by JMA in 2007. RSMC Tokyo has been running a follow-on project from the research outlined in this paper since 2007. Using the AMSU data available in near-real time at MSC, RSMC will validate the method proposed in this paper to distinguish OCCs that will develop into TSs from those that will not, and will try to use other parameters retrieved from the raw brightness temperatures of AMSU channel 7 with the cooperation of JMA/ Meteorological Research Institute. This testbed study was performed using operational EDA. The progress of further research will also be presented in the near future.

9. Summary

Because of the subjective nature of the Dvorak analysis technique, it is necessary to develop an objective method of estimating the intensity of OCCs and detecting the formation of TSs. To this end, we first applied AMSU observational data to the analysis of air temperature profiles within OCCs developing or not developing into TSs over the western North Pacific in 2004. The results of EDA performed by JMA/MSC were introduced to distinguish OCCs developing from those not developing into TSs in this process. Two typical cases of OCC_{TS} and

OCC_L were shown to compare their inner temperature profiles at the upper levels. The OCC_{TS} had larger values and a wider anomaly region than OCC_L, though both clusters had positive anomalies.

As the next step, the temperature anomalies at 200, 250 and 300 hPa near the center of each classified OCC were averaged. For the OCC_{TS}, the average positive anomalies increased along with the T-number estimated using EDA. This tendency was also found in the relationship between the percentages of grid numbers for anomalies of more than 1 K near the centers of the OCC_{TS}, and the average anomalies and the percentage showed peak values at 200 hPa for each T-number of 0.0 - 2.0. On the other hand, the average maximums of the OCC anomalies showed almost constant values for each T-number.

In time series analysis of the temperature anomalies, most OCC_{TS} showed a value of larger than 0.9 K at least once, whereas the anomalies for most OCC_L were below 0.9 K throughout their lifetime. From these analyses, we defined warm core structures within OCCs using an air temperature anomaly threshold of more than 0.9 K in this paper.

Under this definition, warm cores were found in most OCC_{TS} but not in most OCC_L, and 70% of the OCCs with warm cores developed into TSs, while 85% of those with no warm core dissipated without such development. For OCC_{TS} with a warm core, the time from the observation of the warm core by AMSU to identification as a TS was 27.7 hours, meaning that there is a lead time of almost one day in detecting the genesis of TSs. From these results, we can conclude that there is a strong possibility of forecasting cyclogenesis from AMSU observations.

References

Barnes, S. L., 1964: A technique for maximizing details in numerical weather ma analysis. *J. Appl. Meteor.*, **3**, 396-409.

Bessho, K., M. DeMaria and J. A. Knaff, 2006: Tropical cyclone wind retrievals from the Advanced Microwave Sounding Unit (AMSU): Application to surface wind analysis. *J. Appl. Meteor. Climatol*, **45,** 399-415.

Briegel, L. M., and W. M. Frank, 1997: Large-scale influences on tropical cyclogenesis in the western North Pacific. *Mon. Wea. Rev.*, **125,** 1397-1413.

Brueske K. F. and C. S. Velden, 2003: Satellite-based tropical cyclone intensity estimation using the NOAA-KLM series Advanced Microwave Sounding Unit (AMSU). *Mon. Wea. Rev.*, **131,** 687-697.

Cheung, K. K. W., 2004: Large-scale environmental parameters associated with tropical cyclone formations in the western North Pacific. *J. Climate*, **17**, 466-484.

Demuth, J. L., M. DeMaria, J. A. Knaff and T. H. Vonder Haar, 2004: Evaluation of Advanced Microwave Sounding Unit tropical-cyclone intensity and size estimation algorithms. *J. Appl. Meteor.*, **43**, 282-296.

Demuth, J. D., M. DeMaria, and J. A. Knaff, 2006: Improvement of Advanced Microwave Sounding Unit tropical cyclone intensity and size estimation algorithms. *J. Appl. Meteor.*

Climatol, **45,** 1573–1581.

Dickinson, M., and J. Molinari, 2002: Mixed Rossby–gravity waves and western Pacific tropical cyclogenesis. Part I: Synoptic evolution. *J. Atmos. Sci.*, **59,** 2183-2196.

Dvorak, V. F., 1975: Tropical cyclone intensity analysis and forecasting from satellite imagery. *Mon. Wea. Rev.*, **103**, 420-430.

Dvorak, V. F., 1984: Tropical cyclone intensity analysis using satellite data. *NOAA Tech. Rep. NESDIS* 11, Washington, DC, 47pp.

Gierach, M. M., M. A. Bourassa, P. Cunningham, J. J. O'Brien, and P. D. Reasor, 2007: Vorticity-based detection of tropical cyclogenesis. *J. Appl. Meteor. Climatol*, **46,** 1214–1229.

Halverson, J. B., J. Simpson, G. Heymsfield, H. Pierce, T. Hock and L. Ritchie, 2006: Warm core structure of Hurricane Erin diagnosed from high altitude dropsondes during CAMEX-4. *J. Atmos. Sci.*, **63**, 309-324.

Hawkins, H. F., and D. T. Rubsame, 1968: Hurricane Hilda, 1964 II. Structure and budgets of the hurricane on October 1, 1964. *Mon. Wea. Rev.*, **96,** 617–636.

Hawkins, H. F., and S. M. Imbembo, 1976: The structure of a small, intense Hurricane - Inez 1966. *Mon. Wea. Rev.*, **104,** 418–442.

Hawkins, J. D., T. F. Lee, J. Turk, C. Sampson, J. Kent, and K. Richardson, 2001: Real–time internet distribution of satellite products for tropical cyclone reconnaissance. *Bull. Amer. Meteor. Soc.*, **82**, 567–578.

Heymsfield, G. M., J. B. Halverson, J. Simpson, L. Tian, and T. P. Bui, 2001: ER-2 Doppler radar investigations of the eyewall of Hurricane Bonnie during the Convection and Moisture Experiment-3. *J. Appl. Meteor.*, **40,** 1310–1330.

Hoshino, S. and T. Nakazawa, 2007: Estimation of tropical cyclone's intensity using TRMM/TMI brightness temperature data. *J. Meteor. Soc. Japan*, **85**, 437-454.

Katsaros, K. B., E. B. Forde, P. Chang, and W. T. Liu, 2001: QuikSCAT's SeaWinds facilitates early identification of tropical depressions in 1999 hurricane season. *Geophys. Res. Lett.*, **28**, 1043-1046.

Kidder, S. Q., M. D. Goldberg, R. M. Zehr, M. DeMaria, J. F. W. Purdom, C. S. Velden, N. C. Grody, and S. J. Kusselson, 2000: Satellite analysis of tropical cyclones using the Advanced Microwave Sounding Unit (AMSU). *Bull. Amer. Meteor. Soc.*, **81**, 1241-1259.

Knaff, J. A., R. M. Zehr, M. D. Goldberg and S. Q. Kidder, 2000: An example of temperature structure differences in two cyclone systems derived from the Advanced Microwave Sounder Unit. *Wea. Forecasting*, **15**, 476–483.

Knaff, J. A., S. A. Seseske, M. DeMaria and J. L. Demuth, 2004: On the influences of vertical wind shear on symmetric tropical cyclone structure derived from AMSU. *Mon. Wea. Rev.*, **132**, 2503-2510.

Lee, C. C., 1989: Observational analysis of tropical cyclogenesis in the western North Pacific. Part I: Structural evolution of cloud clusters. *J. Atmos. Sci.*, **46,** 2580-2598.

Lee, T. F., F. J. Turk, J. Hawkins, and K. Richardson, 2002: Interpretation of TRMM TMI images of tropical cyclones. *Earth Interactions*, **6**,1-17.

McBride, J. L. and R. Zehr, 1981: Observational analysis of tropical cyclone formation. Part II: Comparison of non-developing versus developing systems. *J. Atmos. Sci.*, **38,** 1132-1151.

Ritchie, E. A., and G. J. Holland, 1999: Large-scale patterns associated with tropical cyclogenesis in the western Pacific. *Mon. Wea. Rev.*, **127,** 2027-2043.

Sharp, R. J., M. A. Bourassa and J. J. O'Brien, 2002: Early detection of tropical cyclones using Seawinds-derived vorticity. *Bull. Amer. Meteor. Soc.*, **83**, 879-889.

Tsuchiya, A., T. Mikawa and A. Kikuchi, 2001: Method of distinguishing between early stage cloud systems that develop into tropical storms and ones that do not. *Geophys. Mag. Series 2*, **4**, 49-59.

Velden, C. S., T. L. Olander and R. M. Zehr, 1998: Development of an objective scheme to estimate tropical cyclone intensity from digital geostationary satellite infrared imagery. *Wea. Forecasting*, **13**, 172-186.

Velden, C. S., B. Harper, F. Wells, J. L. Beven, R. M. Zehr, T. L. Olander, M. Mayfield, C. C. Guard, M. Lander, R. Edson, L. Avila, A. Burton, M. Turk, A. Kikuchi, A. Christian, P. Caroff and P. McCrone, 2006: The Dvorak tropical cyclone intensity estimation technique: a satellite-based method that has endured for over 30 years. *Bull. Amer. Meteor. Soc.*, **87**, 1195-1210.

Zehr, R. M., 1992: Tropical cyclogenesis in the Western North Pacific. *NOAA Tech. Rep. NESDIS* 61, Washington, DC, 181 pp.

Analysis of Tropical Cyclones Using Microwave Satellite Imagery

Jun'ichi ASANO

Meteorological College, Japan Meteorological Agency (JMA)

7-4-81, Asahi-cho, Kashiwa, Chiba, 277-0852 Japan

Shuuji NISHIMURA[i], Koji KATO[ii], Kouki MOURI[iii], Sadao SAITOH,[iv] Shiro YOSHIDA[iii], Takeshi ENDO[v], Kohei OOTUBO[v], Akihiro SHIMIZU[iii], Ryo OYAMA[ii]

Abstract

The Meteorological Satellite Center of the Japan Meteorological Agency has estimated center positions and intensities of tropical cyclones by the *Dvorak method*, which uses infrared and visible imagery from the *MTSAT-1R* geostationary meteorological satellite. While the Dvorak method is the most popular technique for analyzing tropical cyclones through infrared and visible imagery, it is not good at estimating the center positions of tropical cyclones that are covered by upper cirrus cloud and do not have a clear eye in their developing stage, especially during periods when visible imagery is not available.

To combat this difficulty, we used microwave imagery from the *AMSR-E* system on board the *Aqua* earth-observing satellite to analyze the inner structures of tropical cyclones, which cannot be seen in infrared or visible imagery. We also developed a method to estimate center positions of tropical cyclones using this microwave imagery analysis. Verification using the tropical cyclones from 2003 to 2005 showed that the accuracy of center positions estimated by microwave imagery was almost the same as that obtained by radar observation. As a result, our method was proven to be an effective means of improving the accuracy of center positions estimated by the Dvorak method.

[i] National Typhoon Center, Forecast Division, Forecast Department, JMA
[ii] System Engineering Division, Data Processing Department, Meteorological Satellite Center, JMA
[iii] Analysis Division, Data Processing Department, Meteorological Satellite Center, JMA
[iv] Earth Observation Research Center, Japan Aerospace Exploration Agency
[v] Satellite Control Division, Data Processing Department, Meteorological Satellite Center, JMA

1. Principle of Observation with Microwave Imagery

A microwave radiation usually refers to an electromagnetic wave with a frequency of 3 to 30 GHz or a wavelength of 10 to 1 cm (Table 1-1). The frequency range of microwaves for actual observation by satellites includes frequencies that are relatively higher than the range defined in the table, and electromagnetic waves with those frequencies are also called microwaves here for the sake of convenience. Generally, microwave observation equipments are classified according to the observation method and purpose; however, it is generally called a microwave sensor here.

Satellite observation using microwaves requires a frequency range that is significantly lower (or with a longer wavelength range) than that for infrared sensors with geostationary meteorological satellites (10-μm range, which is called the infrared range hereinafter) or for visible sensor (0.6 μm range). Therefore, with limited influence of cloud particles, satellite observation can tell atmospheric conditions under the cloud top. This advantage of microwave sensors that has not been achieved by infrared or a visible sensor presents an absolutely new viewpoint for the analysis of weather phenomena. On the other hand, information that has been accumulated through analysis using infrared and visible imagery may not be applied to analysis with microwaves directly. Therefore, it is important to know the characteristics of the new method with microwaves.

Chapter 1.1 describes the characteristics of microwaves necessary for the analysis of weather phenomena, such as tropical disturbance.

Chapter 1.2 describes classified typical satellites equipped with microwave sensors, and their observation methods.

Chapter 1.3 indicates key points necessary for actual analysis of weather phenomena using imagery produced from observation data obtained with microwave sensors. The same chapter also describes characteristics and provides notes for the wavelength range used for analysis.

For abbreviations in this document, see "Appendix 2 Abbreviations."

Table 1-1 Frequencies, wavelengths, and names of electromagnetic waves

Frequency (Hz)		Wavelength (m)		Name
3×10^{22}		10^{-14}		Gamma ray
3×10^{21}		10^{-13}		
3×10^{20}		10^{-12}		
3×10^{19}		10^{-11}		X ray
3×10^{18}		10^{-10}	(1 Å)	
3×10^{17}		10^{-9}	(1 nm)	
3×10^{16}		10^{-8}		Ultraviolet ray
3×10^{15}		10^{-7}		Visible light
3×10^{14}		10^{-6}	(1 μm)	
3×10^{13}		10^{-5}		Infrared ray
3×10^{12}	(3 THz)	10^{-4}		Submillimeter wave
3×10^{11}		10^{-3}	(1 mm)	Millimeter wave
3×10^{10}		10^{-2}	(1 cm)	**Microwave**
3×10^{9}	(3 GHz)	10^{-1}		
3×10^{8}		1		Ultrashort wave
3×10^{7}		10^{1}		
3×10^{6}	(3 MHz)	10^{2}		Short wave
3×10^{5}		10^{3}	(1 km)	Medium wave
3×10^{4}		10^{4}		
3×10^{3}	(3 kHz)	10^{5}		Long wave
3×10^{2}		10^{6}		Ultralong wave

1.1 Characteristics of the Microwave Range

The microwave range is in a significantly lower-frequency range (or longer-wavelength range) than the visible or infrared ranges (Table 1-1). As with the case of the infrared range, the microwave range acts as the atmospheric window, and is suitable for satellite observation with limited influence of the atmosphere (Figure 1-1). However, the energy within microwave range is significantly small; the scale is a ten-billionth of that of the infrared range. Therefore, satellites equipped with microwave sensors orbit at the altitude (400 to 900 km) significantly lower than geostationary orbit (about 36000 km) to achieve gain (see Chapter 1.2).

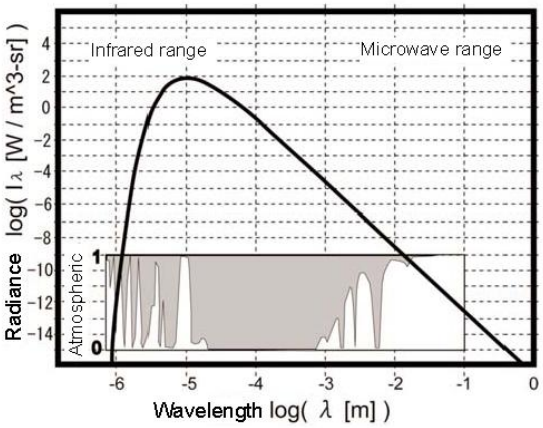

Figure 1-1 Earth radiation spectra and atmospheric transmittance
The radiance of earth radiation is calculated based on the model of a black body of 290 K. For atmospheric transmittance, the height of white spaces corresponds to the strength of a transmittance.

As shown in Figure 1-2, influences by the earth's surface conditions and atmosphere, and various types of particles in the atmosphere, on a microwave depend on its wavelength. This means that it is necessary to select a suitable wavelength to observe a target object. The atmosphere is nearly transparent to a wavelength of 10 GHz or lower. The sea surface temperature is sensitive to the same-wavelength range. The higher the wavelength, the lower the response to the surface temperature. On the other hand, the higher the wavelength, the higher the response to water clouds. Water vapor affects the response of the entire microwave range.

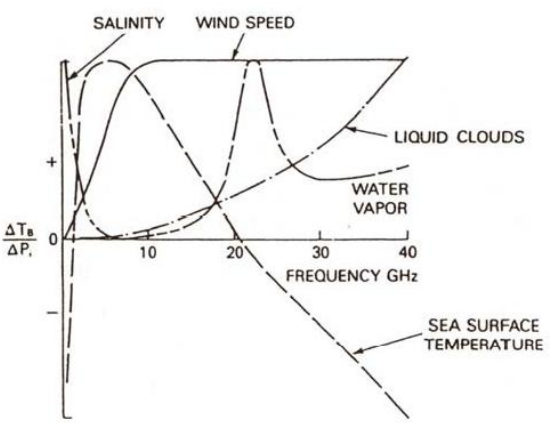

Figure 1-2 Rates of changes in radiation temperature of microwave radiation with respect to various changes in objects to be observed with microwave remote sensing (NASA, 1987)

The following pages describe the general characteristics of microwaves. For characteristics of microwaves not mentioned in this chapter or details on theoretical background, see, for example, Hayasaka (ed., 1996) mentioned in the References.

1.1.1 Atmospheric Influences

Satellite observation of the earth, including that with microwaves, is performed by receiving radiation energy from the earth by satellite sensors, which measure physical quantities with the dimension of energy. Radiation energy emitted from the earth is affected by the air, cloud particles, and raindrops on its way to a satellite sensor. According to usage, energy detected by such sensors is

converted into radiance temperature, or effects of the air on the energy are estimated to retrieve physical quantities.

The microwave range generally has high atmospheric transmittances, so it is easy for microwave radiation from the earth's surface to reach a satellite sensor. This means that information about the surface is easily obtainable.

Microwave radiation with a suitable-frequency transmits clouds, which is nearly opaque to the infrared region, so that conditions inside clouds can be clear. For clouds, satellite observation can tell not only the top using the infrared region, but also the inner structure using the microwave range.

To understand the observation mechanism for the inner structure of clouds, it is necessary to know the influences by cloud particles, raindrops, and snow particles on microwaves. Particles of water and ice absorb, emit, and scatter microwave radiation. The degree of infuluences is greatly different between water and ice particles, and depends greatly on the frequency of an incoming wave.

Generally, water clouds have a high microwave absorptivity, and therefore, a high emissivity. This feature and the low emissivity of the sea surface are reasons for the higher radiation temperature of water clouds than that of the sea surface.

Ice particles such as snow and hail are good scattering bodies of microwaves. This property becomes more significant with an increase in microwave frequency. A high scattering property reduces the volume of radiation that reaches a satellite sensor, leading to lowered radiation temperature. Therefore, well-developed convection clouds in which many ice particles are present above the melting layer are recognized as a region of low radiation temperature, especially in a high-frequency band of the microwave range.

The information given in this section is presented in schematic form as shown in Figure 1-3. Figure 1-3(A) is a schematic diagram of the 89-GHz band.

In the case of A-1, almost the entire radiation emitted by the sea surface is directly observed by a satellite sensor because the influences by high-altitude clouds consisting of ice crystals on microwave radiation are negligible. Water clouds (A-2) absorb and reemit most parts of microwaves emitted by the sea surface. A satellite observes the sum of radiation from the sea surface and water clouds, and the emissivity of water clouds is nearly 1, so the brightness temperature of water clouds is higher than that of the sea surface. In well-developed convection clouds (A-3), radiation is affected by scattering particles such as snow and hail, so the amount of radiation that reaches a satellite is significantly reduced. Therefore, the brightness temperature is also greatly reduced. Figure 1-3 (B) is a schematic diagram of the 36-GHz band. In the case of B-1, a microwave in this band is transmitted through high-altitude clouds in the same way as that in the 89-GHz band. However, the emissivity of the sea surface for the band is significantly low, so its brightness temperature is significantly low. Because microwave radiation in the 36-GHz band is largely reemitted by water clouds (B-2), the brightness temperature of water clouds is higher than that of the sea surface. In well-developed convection clouds (B-3), microwave radiation in the 36-GHz band is scattered, but is not as scattered as that in the 89-GHz band, so the reduction in the brightness temperature is small.

The frequency range of the microwave shown in Figure 1-3 is considered appropriate for tropical disturbance analysis and is described in detail in Chapter 1.3.

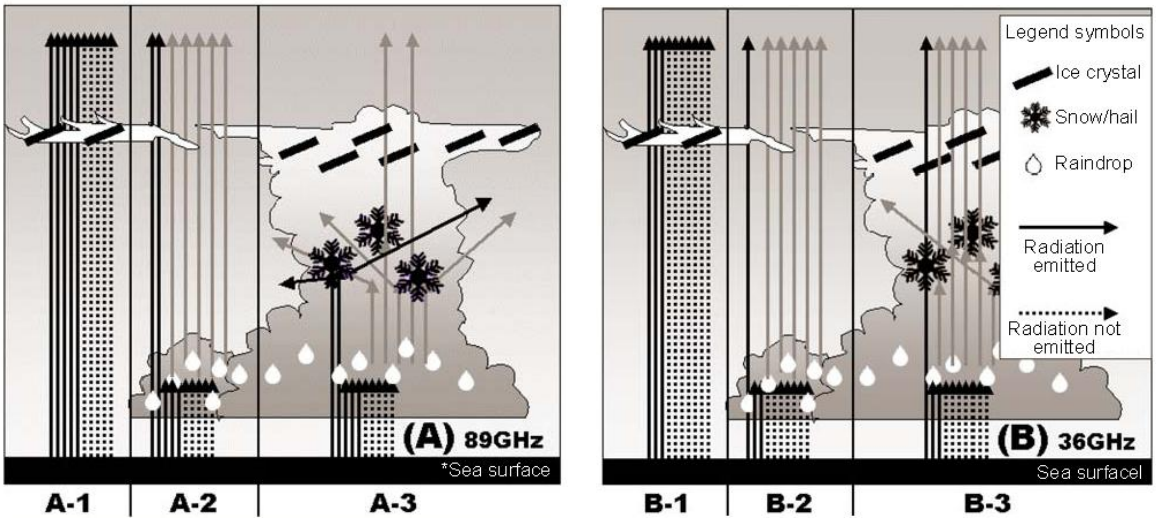

Figure 1-3 Schematic diagram of atmospheric influences on microwave channels

(A) Schematic diagram of 89-GHz band: A-1: Clear weather or clouds only at high altitude; A-2: Water clouds; and A-3: Well-developed convection clouds

(B) Schematic diagram of 36-GHz band: B-1: Clear weather or clouds only at high altitude; B-2: Water clouds; and B-3: Well-developed convection clouds

As the sea emissivity for microwaves is lower than 1, the solid-line arrows indicate radiation actually emitted, and the dotted-line arrows indicate radiation supposed to be emitted if the emissivity is 1. In this diagram, the amount of energy is proportional to the number of arrows. The diagram is prepared supposing no effects of water vapor on the assumption that the sea temperature would be the same. Because the diagram is prepared schematically for easy understanding, the numbers of the arrows in the diagram do not always correspond to actual measurements.

1.1.2 Relationship between the frequency range and horizontal resolution

Wavelengths of the microwave range are in the range of 1 centimeter to 10 centimeters Because the energy of an electromagnetic wave increases in reverse proportion to its wavelength, the horizontal resolution of the shortest-wavelength band (highest frequency) is approximately 10 times higher than that of the longest-waveleng band (lowest frequency) when a wave is observed at the same altitude by an antenna with the same diameter.

Horizontal resolutions of microwave sensors are listed according to their frequencies in Appendix 1 Satellites and Sensors, which shows that the higher the frequency, the higher the resolution.

Such differences in resolution by frequency can be an important factor when you discuss the accuracy of the location of a typhoon eye, for example.

1.1.3 Emissivity of the earth's surface

Generally, an object emits an electromagnetic wave with reference to its temperature. A black body has an emission rate of 1. This means that the radiance temperature calculated using the strength of an electromagnetic wave emitted from the body is equivalent to the temperature of the body itself.

In the infrared region, for example, ground surface, which can be considered a black body, has an emissivity of approximately 1. This suggests that the radiance temperature of unclouded areas in the infrared range is considered to be the temperature of the ground surface.

In the microwave range, on the other hand, the ground surface cannot be considered a black body. Depending on the frequency, the emissivity in the microwave range is basically lower than 1 (Figure 1-4). This indicates that the radiance temperature of the ground observed with a microwave is lower than the actual temperature of the ground surface. This decrease is significant especially on the sea surface, where the emissivity is much lower than 1. This influence is further pronounced on a low-frequency band of the microwave range, with which the radiance temperature of the sea surface is found to be extremely low. Great differences in radiance temperature are observed between the sea surface (extremely low radiance temperature), and water clouds (relatively high radiance temperature achieved by radiation from the clouds, which have an emissivity of approximately 1). Therefore, water clouds appear as regions of high radiance temperature, and can be easily distinguished from the sea surface.

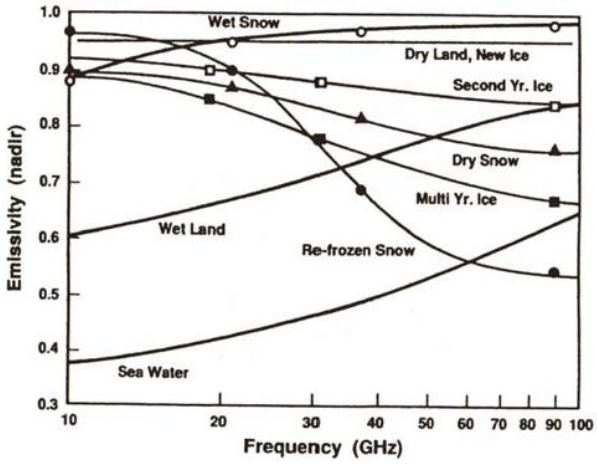

Figure 1-4 Emissivity of different ground surfaces for the microwave range (Grody, 1993)

1.1.4 Polarization (vertical and horizontal)

A microwave is a type of electromagnetic wave and is a transversal wave with its electric and magnetic fields oscillating at right angles to each other (Figure 1-5). An electromagnetic wave whose electric field oscillates at a right angle to the reflection surface (ground surface) is called the vertical polarization. An electromagnetic wave whose electric field oscillates in a plane horizontal to the ground surface is called the horizontal polarization.

Among microwave sensors, many types of imagers measure different polarizations for each frequency.

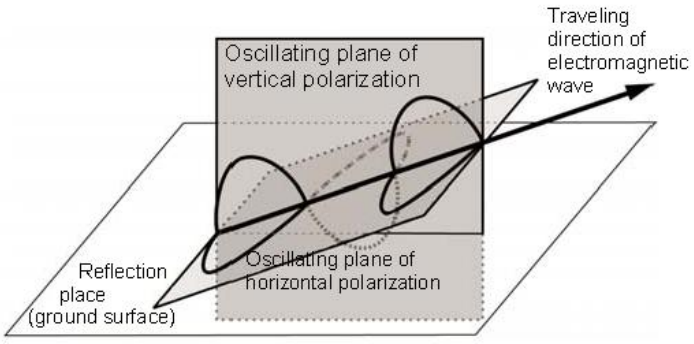

Figure 1-5 Schematic diagram of vertical and horizontal polarizations

Intensities of different components are measured because different components have different properties, which allows estimation of atmospheric influences, especially scattering influences.

On a plane horizontally homogeneous and smooth, the emissivity of a vertical polarization is higher than that of a horizontal polarization because of Fresnel's law and Kirchhoff's law. This means that when a calm sea surface is observed with a microwave, the brightness temperature of a vertical polarization is higher than that of a horizontal polarization. The difference in brightness temperature between these two waves depends on the frequency of a microwave, but the brightness temperature of a vertical wave is always higher than that of a horizontal wave.

If vertical and horizontal polarizations are affected by scattering particles on their way to a satellite sensor, scattering changes the oscillating direction of the electric field of a wave in various directions. Therefore, scattering effects on a microwave decreases the difference in brightness temperatures between its vertical and horizontal polarizations. Using this property, it is possible to distinguish between the sea surface and well-developed convection clouds using a measurement of radiance temperature for the region.

1.2 Types of microwave sensors and satellites

1.2.1 Orbits of satellites equipped with a microwave sensors

Satellites equipped with a microwave sensor orbit at an altitude of approximately 400 to 900 kilometers. They take 90 to 100 minutes to make an orbit of the earth. Unlike geostationary meteorological satellites, which are in stationary orbit of the earth and take images of the same area, many satellites equipped with a microwave sensor make an orbit of the earth in a short cycle, and observe strip-shaped areas several-thousands-kilometer wide, as described on the next section.

Because this observation method limits the area that can be observed while a satellite make an orbit, in most cases, a slight change is made to a satellite's orbit when it has made an orbit so that images taken in different orbits cover almost the entire earth. Many satellites orbit over both poles of the earth. Such orbits are called polar orbits, and satellites that take polar orbits are called polar orbiter. Typical polar orbiters equipped with a microwave sensor include the Aqua satellite, DMSP satellite series, and NOAA satellite series. These satellites orbit the earth while keeping the angle between their orbital planes and orientations toward the sun the same. Such orbits are called sun-synchronous orbits. Its advantage is that an area can be observed twice a day at the same local times. This reduces the influences of changes in sunlight.

An orbit in which a satellite returns to its starting point within 24 hours after it has made some orbits is called a recurrent orbit. An orbit in which a satellite returns to its starting point after more than 24 hours and within several days is called a sub-recurrent orbit. Most polar orbiters take the sub-recurrent orbit because the coverage of satellites is wide and they return to the starting point regularly.

In summary, the above-mentioned orbit of polar orbiters can be called the sun-synchronous

sub-recurrent orbit. This orbit possesses many advantages: a satellite in this orbit returns to the starting point in a cycle of several days while it observes the same area at the same local time under the same conditions where a satellite keeps its positional relationship with the sun the same.
On the other hand, the TRMM satellite does not take the polar orbit. The angle between the satellite's orbit plane and the equatorial plane is 35 degrees. It observes the area ranging between 35 degrees north and 35 degrees south of the equator. This satellite is not sun synchronous because it observes day changes in the rainfall in the tropical region at different local time.

1.2.2 Passive and Active Sensors

Satellite observation with a microwave is roughly classified into two according to the sensor types: a passive sensor or an active sensor.

A passive sensor receives microwave radiation that is emitted naturally from the earth. This is the same observation mechanism as for infrared imagers for geostationary meteorological satellites. As mentioned in the first part of this section, the energy of the microwave range by earth radiation is very small. Generally, the energy received by an antenna is proportional to its diameter, and inversely proportional to the distance to the observation object. Therefore, in order to achieve gain, satellites are orbited at a low altitude or equipped with a large antenna. However, despite these efforts, the temperature resolution of passive sensors is still lower than that of infrared imagers.

Typical passive sensors for the microwave range are: AMSR-E, loaded on the Aqua satellite; SSM/I, loaded on the DMSP satellite series; TMI, loaded on the TRMM satellite; and AMSU-A, AMSU-B, and MHS, loaded on the NOAA satellite series. Data obtained with these passive sensors are used to analyze weather phenomena using their brightness temperatures. This is described in detail later.

An active sensor itself emits a microwave like a radar, and observes a wave reflected by an object. For example, SeaWinds, loaded on the QuikSCAT satellite, measures the direction and speed of winds over the sea by detecting the scattering state of a microwave, which is scattered in a different way according to the sea surface state. The TRMM satellite has a 14-GHz precipitation radar to observe precipitation. The CloudSat satellite has a 94-GHz radar to detect the three-dimensional structure of clouds. As represented by these examples, an active sensor is used to obtain specific physical products, such as wind or rain.

1.2.3 Imager and sounder

As with an infrared sensor, a microwave passive sensor is classified into an imager and a sounder.

An imager is observational equipment to covert data into images with a relatively high horizontal resolution. Typical imagers include: AMSR-E, loaded on the Aqua satellite; SSM/I, loaded

on the DMSP satellite series; and TMI, loaded on the TRMM satellite. For each observation frequency, these imagers observe its vertical and horizontal polarizations, which are described in Chapter 1.1.4, and convert obtained data into images.

A sounder is equipment to observe different frequencies in order to obtain vertical profiles of physical quantities for a purpose, such as air temperature distribution and water vapor distribution. A sounder is configured to observe many frequencies at and around a specific absorption line according to a physical quantity to be obtained. For its high wavelength resolution, a sounder trades off horizontal resolution. Generally, a sounder has a lower horizontal resolution than an imager. Typical sounders of microwave sensors are AMSU-A, AMSU-B, and MHS, loaded on the NOAA satellite series. AMSU-A is designed to obtain temperature profiles, while AMSU-B and MHS are designed to obtain vertical water vapor profiles.

Unlike an imager, a sounder is designed mainly to obtain vertical profiles of physical quantities, so it observes either a vertical polarization or a horizontal polarization.

To analyze a meteorological phenomenon using its graphic information, an imager is more suitable. It is possible to use a sounder using a selected frequency in the same way as an imager, but a lower horizontal resolution than that of an imager is produced. A sounder has a disadvantage in that polarization information is unavailable. Observation with a microwave sensor is performed with insufficient frequency, so the use of microwave data obtained with a sounder is of value.

1.2.4 How to Scan with Microwave sensors

There are two main modes of antenna scanning to observe the earth with a microwave sensor: the conical scanning, and the cross-track scanning.

Conical scanning is a mode of scanning by antenna rotation on the base of a satellite as shown in Figure 1-6. This mode is named “conical scanning” because an antenna at a constant angle with respect to the vertical direction moves in a conical form while scanning the ground. Because conical scanning observation keeps the angle that the antenna forms with ground the same, the size of FOV (Field Of View: the area that a sensor can view at one time) is constant during observation, so that the angular characteristics of radiation are maintained. Therefore, the conical scan mode is used in many types of microwave imagers that observe both the horizontal and vertical polarizations, including all of the imagers mentioned in the previous section. Because of the constant antenna angle, the swath

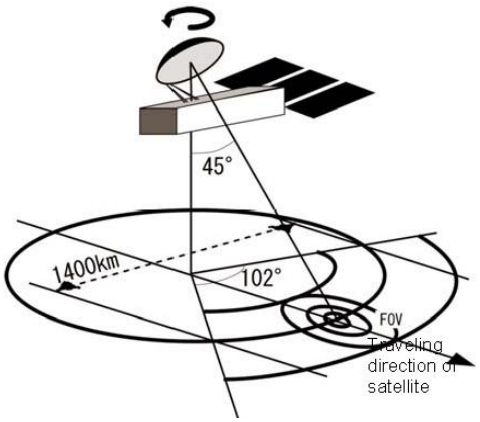

Figure 1-6 Schematic diagram of conical scanning
The concept of conical scanning is represented graphically, using SSM/I as an example.

width is lower than that for the track scanning mode. Figure 1-6 shows an example of SSM/I. Among nested FOVs, an FOV that is closer to the center of the nest is dedicated to observation of a higher frequency, and a higher resolution is produced by a higher frequency.

Cross-track scanning is a mode of scanning by antenna movement along the direction perpendicular to the traveling direction of a satellite. Therefore, the FOV is minimal at the point at which the satellite observes directly below it, and is greater at a position that is further from the minimal position. Because the angle that the antenna forms with the ground is changed, angle characteristics are not maintained. On the other hand, the swath width of the cross-track scanning can be greater than that of the conical scanning. Most sounders adopt cross-track scanning. The cross-track scanning mode is used in all sounders mentioned in the previous section. As shown in Figure 1-7, prepared using AMSU-A and -B as examples, the FOV of AMSU-B, dedicated to observation with a higher frequency, is inside the FOV of AMSU-A.

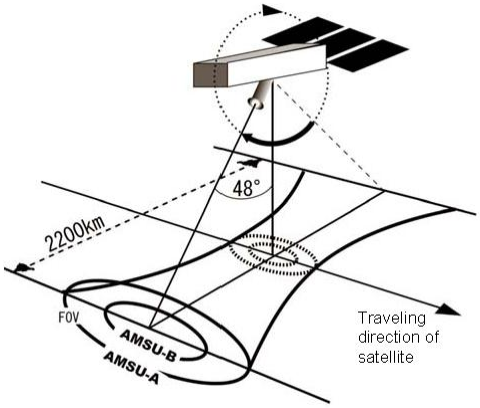

Figure 1-7 Schematic diagram of cross-track scanning
The concept of cross-track scanning is presented schematically, using AMSU-A and -B as examples.

1.3 Analysis with microwave imagery

This section describes important things for analyzing meteorological phenomena based on the properties of microwaves and characteristics of the observation method.

As shown in "Appendix 1 Satellites and Sensors," a microwave sensor uses many frequencies for observation. However, not all data converted into graphic data are suitable for the analysis of meteorological phenomena. Therefore, it is necessary to select frequencies suitable for the operational application of tropical disturbance analysis (Kato et al., 2004) performed at the Meteorological Satellite Center.

This section describes an analysis with frequencies used in surveys described in Chapter 2 or later. Frequency bands are named from the observation frequencies of AMSR-E. Slightly different frequencies are used in other sensors for observation (e.g., 89 GHz is used for AMSR-E, while 85.5 GHz is used for SSM/I). Observation frequencies are different according to the sensor, but are selected essentially within the frequency band that has the same characteristics. Differences in observation frequencies selected in this way have few effects on the analyses described later, so the same name is given to the selected observation frequencies for the sake of convenience.

The 89-GHz and 36-GHz bands are selected to analize tropical cyclones. In next section and later, their characteristics are described based mainly on advantages and disadvantages for analysis.

However, interpretation of microwave images is under development, and many aspects remain insufficiently revealed. It should be noted that with preceding studies, such as those by Randall et al. (1992 and 1993), as a guide, characteristics of selected frequencies are extracted and described based on frequencies and actual radiation temperature distributions that have been illustrated.
Points to consider for tropical disturbance analysis are mainly provided after description of the two selected frequency bands

1.3.1 Characteristics of the 89-GHz band

The 89-GHz band is a relatively high-frequency band of the microwave range with a relatively high horizontal resolution (about 6 kilometers for AMSR-E). The main characteristic of the band is that it is greatly scattered by ice particles such as snow or hail. Therefore, well-developed convection clouds are found to be areas of extremely low radiance temperature (c1 and c2 areas in Figure 1-9).

Based on this property, especially in tropical disturbance analysis, the area of the strongest convection stands out in a well-developed convection cloud such as the Cb band, and is easily identifiable.

Other characteristics can be explained by the previously described properties of the microwave.

As compared with the land (with an emissivity of about 1), the sea surface (with an emissivity of lower than 1) is found to be a region of lower radiation temperature (around b1 and b2 in Figure 1-9). Because of absorption and scattering by water cloud particles or raindrops, water clouds below the melting layer are found to be a region of relatively higher radiation temperature than that of the sea surface (around e1 and e2 in Figure 1-9).

Using these characteristics, the main analytical work using these frequency bands is tracking of areas of low radiation temperature of well-developed convection clouds. Generally, it is useful to limit the object to be observed with a microwave to the sea surface. However, because well-developed convection clouds stand in sharp contrast to the land, which appears as a region of high radiation temperature, it is possible to keep track of such clouds over the land.
It should be noted that well-developed convection clouds and a sea surface with low surface temperature may be confused because their radiation temperature is found to be similar. For example, a typhoon over a sea area with low surface temperature should be carefully analyzed.

To avoid this kind of confusion, a good method is comparison of radiation temperature between the vertical and horizontal polarizations. If a microwave is sufficiently scattered in a convection cloud, the radiation temperature of the vertical polarization will be nearly the same as that of the horizontal polarization. Therefore, well-developed convection clouds are distinguishable from the sea surface, which makes a great difference in radiation temperature between the vertical and horizontal polarizations of a microwave.

An example of this is shown in Figure 1-8. In Figure 1-8 (A) of infrared imagery, no clouds are observed over the Yellow Sea or sea area in the southern part of Okinawa. The radiation temperature

is about 283 K and 293 K, respectively, which makes a difference of about 10 K. Looking at the microwave imagery of Figure 1-8 (B) and (C), the brightness temperature of the Yellow Sea is found to be much lower than that of the sea area in the southern part of Okinawa, and almost the same as that of the convection cloud accompanied by Typhoon No. 200601 around the Philippines. These figures clearly show some change in radiation temperature between the vertical and horizontal polarizations in the region of low brightness temperature caused by the active convection cloud accompanying the typhoon. And in the Yellow Sea, the brightness temperature of the horizontal polarization is lower than that of the vertical polarization, which makes a great difference between them.

Another effective discrimination method is the use of polarized corrected temperature (PCT) (Spencer et al. 1989). Using calculated PCT values, effects of polarization by the sea surface or water drops can be eliminated to extract a decrease in radiation temperature by scattering, so that convection clouds are easily identifiable. The Meteorological Satellite Center provides calculated results of different radiation temperatures, including PCTs, in real time, but this service is in the trial-and-error stage.

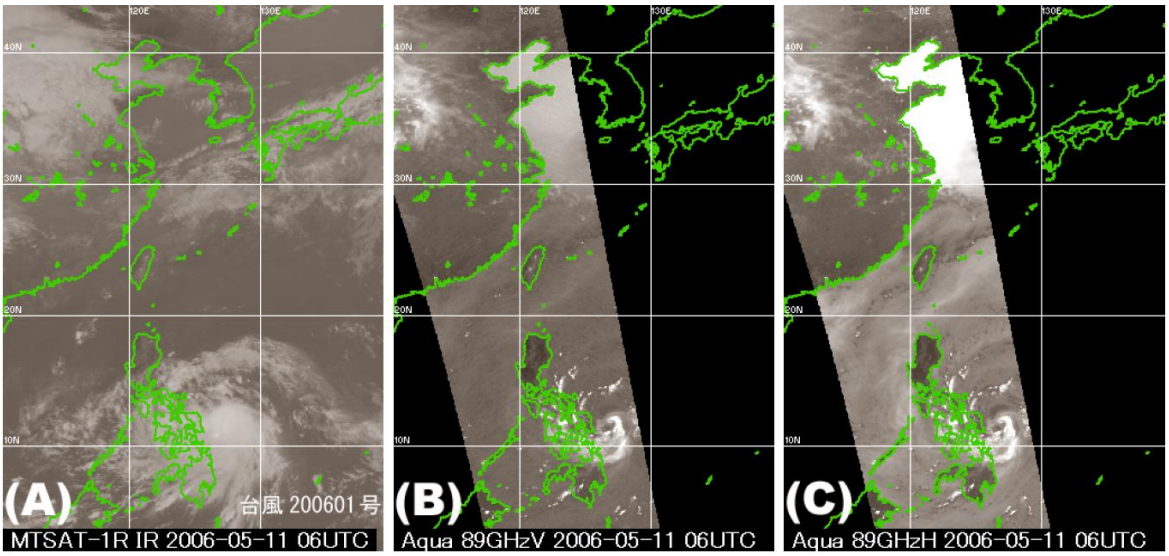

Figure 1-8 Images of vertical and horizontal polarizations of the 89-GHz band (06 UTC, May 11, 2006)
(A) Infrared image, (B) Vertical polarization, and (C) Horizontal polarization
In each image, a darker region (blacker) indicates a region of higher brightness temperature, and a lighter region (whiter) indicates a region of lower brightness temperature.

1.3.2 Characteristics of 36 GHz

The 36-GHz band is a middle-frequency band of the microwave range with a lower horizontal resolution than that of the 89-GHz band (about 14 kilometers for AMSR-E). The main characteristic of the band is that the sea surface is found to be a region of low radiation temperature, and microwaves are strongly affected by water clouds. Because absorption and emission by precipitation

particles and cloud particles affect microwaves in the 36-GHz band more strongly than in other frequency bands, water clouds are found to be a region of high brightness temperature (f3 and f4 areas in Figure 1-9). The sea surface is found to be a region of extremely low radiation temperature because of the low emission rate (around b3 and b4 in Figure 1-9).

These characteristics allow identification of water clouds over the sea as a region of high brightness temperature with high contract, so detection of water clouds over the sea is the main analytical work using the 36-GHz band. However, observation of water clouds over the land is impossible because the emissivity of the land is high and the radiation temperature is high.

It should be noted that in some cases, effects of scattering by ice particles such as snow or hail on the 36-GHz band are not negligible. A decrease in the radiation temperature of this band is not negligible for extremely well-developed convection clouds such as a typhoon. In this case, it is necessary to distinguish whether a region of low radiation temperature comes from the sea surface or a convection cloud. To distinguish these differences, it is effective to use polarization data, as described in the section of the 89-GHz band (see Chapter 1.3.3). A region with a great difference in radiation temperature between the vertical and horizontal polarizations suggests the sea surface and a region with a small difference suggests a well-developed convection cloud.

1.3.3 Microwave imagery comparison

Using Figure 1-9, characteristics of the 89-GHz and 36-GHz bands are explained through comparison of graphical representation between them. In this section, Figures 1-9 (A) to (E) are abbreviated to (A) to (E), respectively.

Two cloud masses clearly shown in the infrared image (A) indicate typhoons: the one over the sea area in the southern part of the major island of Japan is numbered 200607, and the other at a latitude of approximately 20 degrees north is numbered 200608. Infrared image (A) shows a case example in which analyses of the eyes of Typhoon Nos. 200607 and 200608 are difficult.

In microwave images (B) to (E), the land surface (e.g., a1 to a4 of each image) exhibits the highest radiation temperature, and appears as dark areas. The sea surface (e.g., b1 to b4 of each image) appears as dark areas (b1 and b2) with the 89-GHz band having a relatively high emissivity, and as light areas (b3 and b4) with the 36-GHz band having a low emissivity. On the sea surface in each frequency band, vertical polarization (b1 and b3) is higher in brightness temperature than horizontal polarization (b2 and b4), and the sea surface appears as dark areas. The sea surface exhibits a great difference in radiation temperature between the horizontal and vertical polarizations.

In images (B) and (C) of the 89-GHz band, areas (e.g., c1 and c2) of active convection clouds affected by scattering by ice particles over the melting layer are extremely low in radiation temperature, and appear as glistening white. In Typhoon No. 200608, an area of high radiation temperature at a latitude of 20 degrees north suggests its eye (d1 and d2). Concerning Typhoon No. 200607, water clouds (e1 and e2) appear as relatively dark areas that are warmer than the sea surface

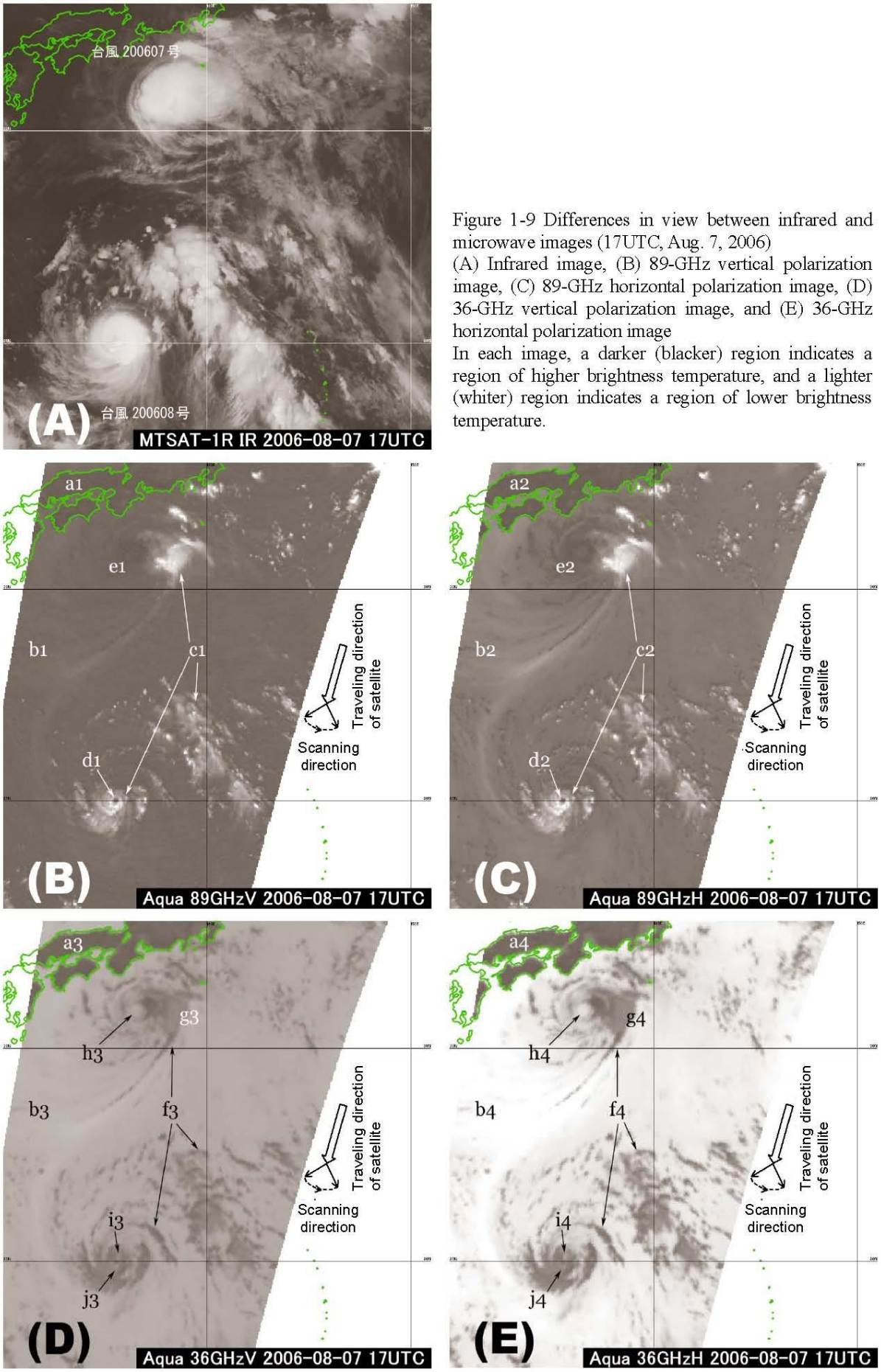

Figure 1-9 Differences in view between infrared and microwave images (17UTC, Aug. 7, 2006)
(A) Infrared image, (B) 89-GHz vertical polarization image, (C) 89-GHz horizontal polarization image, (D) 36-GHz vertical polarization image, and (E) 36-GHz horizontal polarization image
In each image, a darker (blacker) region indicates a region of higher brightness temperature, and a lighter (whiter) region indicates a region of lower brightness temperature.

location of the eye.

In images (D) and (E) of the 36-GHz band, both typhoons are increased in radiation temperature in the water cloud regions (e.g., f3 and f4), and are darker than the sea surface. The important point to note is that well-developed convection clouds (e.g., g3 and g4) look lighter than regions of only water clouds because many the ice particles in the upper water clouds decrease the brightness temperature, although the amount of decrease is not as significant as in the case of the 89-GHz band. In the 36-GHz band images, the eye of Typhoon No. 200607, which is difficult to locate in the 89-GHz band images, can be located as the center (h3 and h4) of a lower vortex of water clouds. The eye of Typhoon No. 200608 appears as an off-white region (i3 and i4) near the north side of the 20th parallel north of the equator. A difference in position of approximately 10 kilometers originates with a parallax error, which is described in the next section. Other white areas (j3 and j4), which are confusing, are observed on the south side of the 20 degrees north. Area i3 looks darker than area i4 with a great difference in radiation temperature between the vertical and horizontal polarizations. This suggests that areas of low brightness temperature of the region are the sea surface. On the other hand, no difference in radiation temperature between areas j3 and j4 is observed, which suggests that the decrease in radiation temperature is caused by scattering particles in an extremely well-developed cumulonimbus cloud. Like these examples, comparison of brightness temperature between the vertical and horizontal polarizations can avoid confusion.

1.3.4 Important Points on Analysis with Microwave Imagery

Because of the basic properties of microwaves, the 89-GHz and 36-GHz bands have the advantage that images taken with these bands provide information about areas under high-level clouds, which is unknown on infrared or visible images. As previously described, however, their main objects to be analyzed are different, so it is important to use the advantages of both bands to complement each other. However, images of these bands have the disadvantages described below, so infrared or visible images should be used, if necessary.

The altitude to be observed differs between the 89-GHz and 36-GHz bands. The 89-GHz band is used to observe active convection areas over the melting layer, while the 36-GHz band is for water clouds below the layer. If a disturbance such as a typhoon is observed using these bands, a broad area of water clouds can be observed with the lower-frequency band, while an area of active convection in the water clouds is observed with the other band.

This difference in the altitude to be observed between both bands exerts an influence mainly on analyses of typhoon eyes. Cloud walls surrounding a typhoon eye tend to be larger in higher altitude. Therefore, a typhoon eye is observed at a high altitude with the 89-GHz band, and the area of the eye is found to be larger than an area observed with the 36-GHz band (Figure 1-10). Using this low-frequency band, a typhoon eye is observed at a low altitude, and is found to be smaller in area

than one using the high-frequency band (Figure 1-10). However, the resolution of the 36-GHz band is lower than that of the 89-GHz band, and the outer edges of water clouds frequently appear as unclear, so comparison between both images is necessary for analysis.

Another important point to note is that as described in Chapter 1.2.4, a microwave imager observes the surface of the earth at an angle (incident angle of approximately 55 degrees) by conical scanning. In the location of a typhoon eye, a deviation is observed, as shown in Figure 1-11. This difference is called a parallax error. The parallax error of the 89-GHz band, the detection range of which is at a higher altitude than that of the 36-GHz band, is larger than that of the 36-GHz band. Naturally, a parallax error is produced even with the 36-GHz band, so it is necessary to correct these differences to the extent possible.

However, it is difficult to estimate the degree of the parallax error for each band because the altitude with the highest detection range of a band depends on the vertical structure of clouds or atmospheric profiles at any given time. Using the 89-GHz band, a satellite observes an area around the tropopause at a certain altitude distribution of scattering particles, producing a disparity of approximately 20 kilometers.

If an analysis finds a deviation in the location of the typhoon eye between the 89-GHz band and 36-GHz band images, the first cause to be suspected is a parallax error. To correct this, it is necessary to consider the traveling direction of a satellite on the orbit and the orientation of the sensor.

As mentioned so far, analyses using microwave images provide useful pieces of information, but they are not always effective. Concurrent use of infrared or visible images will produce better results. If analyses using infrared or visible images are difficult, a microwave image should be used to know the inner structure of disturbance. If a microwave image provides insufficient information, comparison with analytical results using infrared or visible images is necessary. To fill the information gap of each image, it is necessary to use the advantages of different types of images.

In closing, characteristics of the 89-GHz and 36-GHz bands are listed in Table 1-2. Based on the characteristics of microwave images described so far, the survey mentioned in Chapter 2 is conducted.

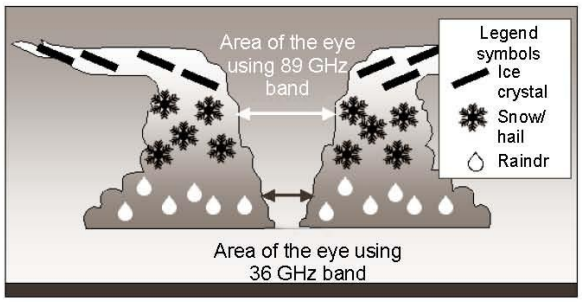

Figure 1-10 Schematic diagram of the observation altitude of a typhoon eye using different frequency bands

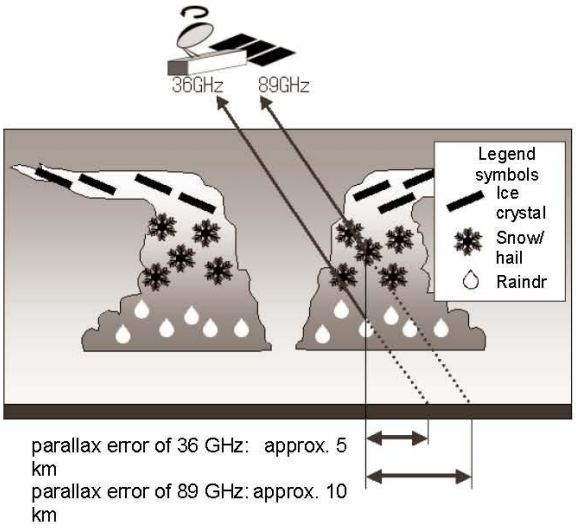

Figure 1-11 Schematic diagram of parallax error

Table 1-2 Characteristics of 89-GHz and 36-GHz bands
A circle sign shows a suitable characteristic for disturbance analysis for the frequency band.
An × sign shows an unsuitable or noteworthy characteristic for analysis for the frequency band.

36 GHz Band	**89 GHz Band**
○ Can analyze the structure of a typhoon under high-altitude clouds	
× Lower resolution compared with 89 GHz band	**○ Higher resolution compared with 36 GHz band**
○ Suitable for detection of water clouds or precipitation areas	**○ Suitable for detection of well developed convection clouds**
× Cannot clearly distinguish between land and clouds	Δ Can track convection clouds over the land
	× Can confuse between cold sea surface and convection clouds
○ Smaller parallax error compared with 89 GHz band	× Larger parallax error compared with 36 GHz band
○ Observe a smaller size of a typhoon eye at low altitude	× Observe a larger size of a typhoon eye at high altitude

2. Tropical disturbance analysis using microwave imagery

2.1 Overview

Microwave imagery obtained with the AMSR-E sensor loaded on the Aqua polar orbiter has been available since June 2003. Taking this opportunity, the Analysis Division of the Meteorological Satellite Center has conducted research and technological development for application of such imagery to tropical disturbance analysis. Analyses of typhoon eyes using microwave imagery have already been conducted by, for example, Lee et al. (2002), who provided qualitative information only. We focused our study on the development of an analytical method that is as quantitative as possible, and developed a new analytical method for typhoon eyes using microwave imagery. Our newly developed method was compared with the radar weather report method, such as RADOB, to study analytical parameters, such as precision.

2.2 Study Period

June 2003 to December 2005

2.3 Tropical disturbance to be analyzed

Our analysis targets are microwave imagery of tropical disturbance obtained during our study period. They are listed in Table 2-1.

2.4 Analysis items

a. Pattern-specific occurrence rate using imagery

Different images are obtained for the same tropical disturbance between microwave imagery and visible/infrared imagery. In our study, therefore, we classified the cloud

Table 2-1 Tropical disturbance analyzed
For the TC numbering, see Appendix 2 "Abbreviations."
Figures in parentheses indicate numbers that could be analyzed.

Year 2003

TC0007(2)	TC0017(6)	TC0029(2)
TC0011(1)	TC0020(12)	TC0030(1)
TC0012(8)	TC0021(8)	TC0031(15)
TC0015(1)	TC0025(1)	
TC0016(6)	TC0026(4)	

Year 2004

TC0003(14)	TC0015(8)	TC0027(2)
TC0004(8)	TC0016(1)	TC0031(12)
TC0006(4)	TC0018(8)	TC0032(6)
TC0007(7)	TC0019(5)	TC0033(8)
TC0008(3)	TC0020(7)	TC0034(11)
TC0009(8)	TC0021(16)	TC0035(11)
TC0010(8)	TC0022(8)	TC0037(7)
TC0011(11)	TC0023(1)	TC0040(5)
TC0012(4)	TC0024(16)	
TC0013(8)	TC0025(4)	

Year 2005

TC0001(5)	TC0009(7)	TC0017(11)
TC0002(6)	TC0010(3)	TC0018(8)
TC0003(8)	TC0011(10)	TC0019(5)
TC0004(13)	TC0012(10)	TC0020(15)
TC0005(12)	TC0013(7)	TC0021(8)
TC0006(7)	TC0014(13)	TC0022(8)
TC0007(6)	TC0015(12)	TC0023(7)
TC0008(5)	TC0016(2)	

pattern of tropical disturbance on microwave imagery into three empirical types, and studied the occurrence rate of each type.

b. Analytical precision for tropical disturbance

The distance between the eye of a tropical disturbance analyzed using microwave imagery and that using visible/infrared imagery, and their latitude and longitude errors are studied. Using RADOB reports that provide precise positional information as independent data, distances from eyes obtained by analysis on microwave imagery and latitude and longitude errors are studied to determine the precision of our analytical method.

c. Comparison of imagery between microwave and visible/infrared

Measurement items in traditional tropical disturbance analysis using visible and infrared imagery include "eye precision." This information suggests the diameter of an area in kilometers, in which the eye of a tropical disturbance exists with a 90 percent probability. In our study, using the traditional measurement method of eye precision as a guide, a new measurement method suitable for precision of our microwave imagery analysis is defined, and measurement is performed using the new method. Our newly defined item is called the eye analysis size in this document. Values obtained using microwave imagery are compared with those obtained using traditional visible/infrared imagery.

On a man-machine interface, a qualitative evaluation is also performed on microwave imagery and visible/infrared imagery to check which imagery provides clearer and easier-to-understand information.

2.5 Analytical procedures

A microwave image of a tropical disturbance is analyzed in the following steps and order: pattern selection; eye analysis; measurement of eye analysis size; and comparison between microwave imagery and visible/infrared imagery (Figure 2-1).

In pattern selection, a cloud pattern in microwave imagery is determined based on the criteria of the chart in Figure 2-1. After this step, an "eye analysis" and "eye analysis size" measurement are performed based on the methods for the selected pattern. If a cloud pattern is found to be "unknown," these analyses are not performed.

"Comparison between microwave imagery and visible/infrared imagery" offers seven options, among which an analyzer selects an appropriate one. The options and selection conditions are listed in Table 2-2.

Based on the characteristics and resolution of chanels, 89 GHz and 36 GHz are selected as analysis chanels. Vertical polarization is used because of its high emissivity. Basically, only images of tropical disturbance over the sea are analyzed. Images of disturbance over the land are not analyzed because the decrease in contrast between the disturbance and the land surface resulting from a higher

emissivity from the land surface than from the sea surface often makes analyses difficult. A quality control (QC) value of 2 degrees is set as a threshold value for statistical work of analytical results to determine the distance between two points and the latitude and longitude errors of two points. If the latitude and longitude error of two points is 1.9 degrees, the data are accepted. If the error is 2.1 degrees, the data are rejected, for exapmle. This acceptance/rejection criterion is set so as not to analyze the wrong data in the case of more than one disturbance in close proximity to each other. The value is based on a distance of about 2 degrees at 20 degrees north latitude, which is converted from an accuracy of constant 175 kilometers for the Cb cluster pattern in traditional visible/infrared imagery analysis.

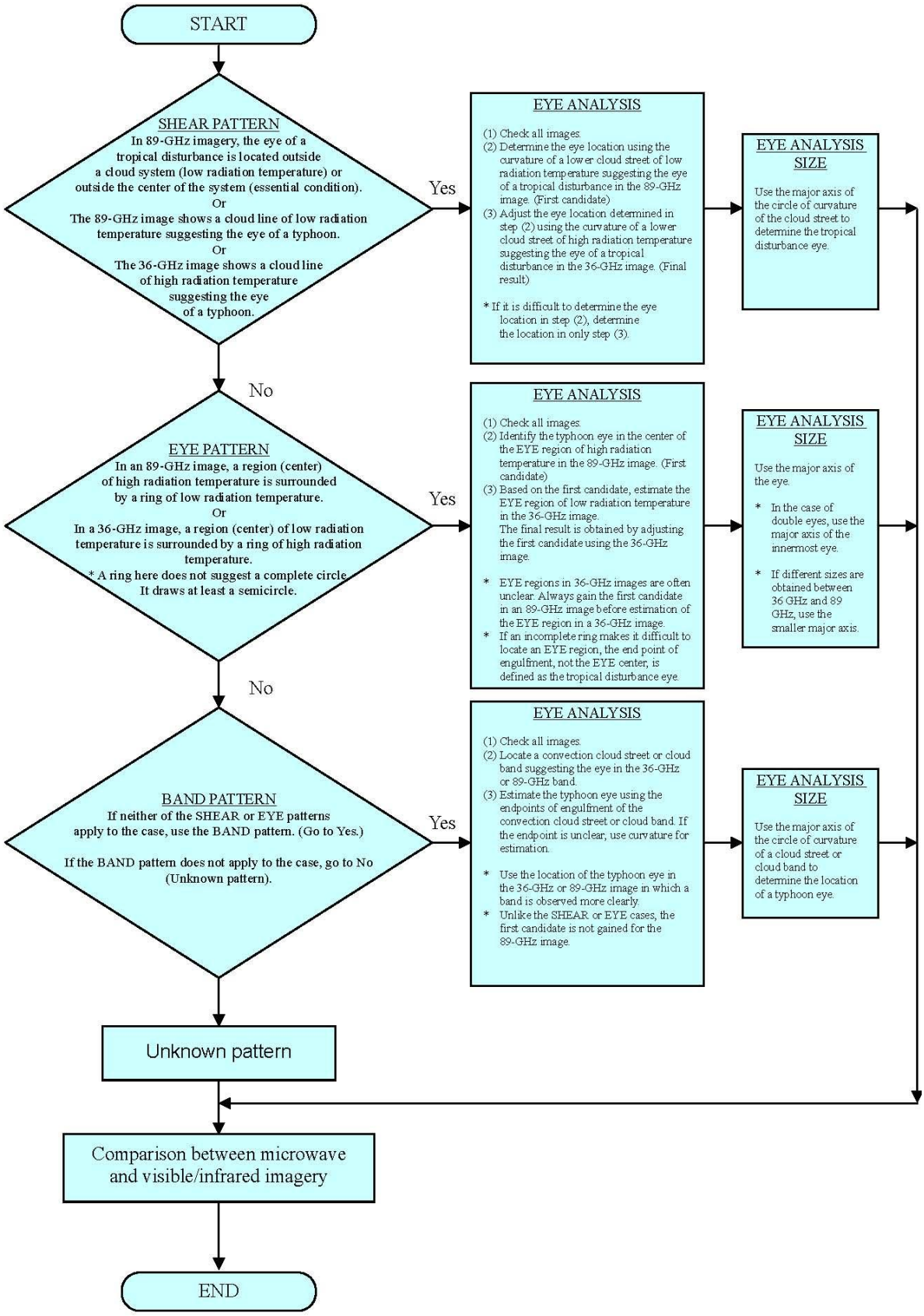

Figure 2-1 Flow chart of analytical procedures

Table 2-2 Options and criteria for comparison between microwave and visible/infrared imagery

Option	Condition	Remarks
Microwave imagery is clearer.	The eye is located clearly in the EYE pattern on microwave imagery. Other than EYE pattern in visible/infrared imagery	
	The eye is clearly located in the BAND or EYE pattern in microwave imagery. Difficult to locate the typhoon eye in visible/infrared imagery	
Microwave imagery is slightly clearer.	EYE pattern in microwave imagery The eye is clearly located in other than the EYE pattern in visible/infrared imagery.	Clearness of eye location in visible/infrared imagery is based on the ability of location of a typhoon eye without seeing moving images.
	The typhoon eye is clearly located in a clear BAND in other than the EYE pattern in microwave imagery. Typhoon eye is located unclearly in visible/infrared imagery	
Microwave and visible/infrared imagery are both unclear.	Unknown pattern in visible/infrared and microwave imagery, and difficult to locate the typhoon eye	Select in the case of UNDEFINED for visible/infrared imagery or unknown pattern for microwave imagery. Useful for SHEAR on extremely unclear images
Microwave and visible/infrared imagery are both clear.	EYE in both visible/infrared and microwave imagery	
Visible/infrared imagery is slightly clearer.	The typhoon eye is located unclearly in BAND or SHEAR in microwave imagery. The eye is clearly located in visible/infrared imagery.	The eye is located unclearly in both visible/infrared and microwave imagery, but can be located in visible/infrared imagery.
Visible/infrared imagery is clearer.	Unknown pattern in microwave imagery and unclear typhoon eye location Clear or slightly clear eye location in visible/infrared imagery	Select in the case of unclear cloud streets in the SHEAR pattern in microwave imagery.
Unknown	Peculiar images, and not included in the above classification	

* Use the Dvorak method as the analytical method for tropical disturbance in visible/infrared imagery.

2.6 Cloud patterns in microwave imagery

In our study, a suitable cloud pattern in microwave imagery is selected among the following three options.

a. SHEAR pattern
b. EYE pattern
c. BAND pattern

These are patterns empirically determined based on convection cloud streets and eyes of tropical disturbances. Their names are the same as those of the Dvorak method, but given slightly different definitions for our classification because vision in microwave imagery differs from that in visible/infrared imagery (Figure 2-1). Characteristics of the three patterns and measurement methods of "Eye Analysis" and "Eye Analysis Size" are described using actual images.

a. SHEAR pattern

A schematic diagram of the SHEAR pattern is shown in Figure 2-2a. A characteristic of this pattern is that the eye of a tropical disturbance is away from the cloud zones where disturbances are developed. Cloud zone A is a cloud system of a tropical disturbance, and appears as a well-developed cloud zone of low radiation temperature on 89-GHz imagery. Cloud zone B is a frontal cloud band. Although this band is not always accompanied, it is often accompanied in the northern part of the mid-latitude region. Convection cloud street C is seen with relatively high

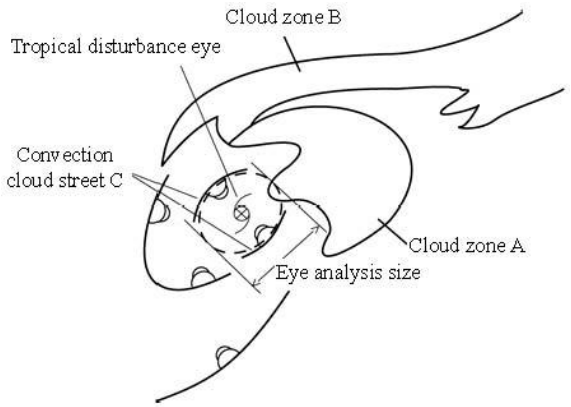

Figure 2-2a Schematic diagram of the SHEAR pattern

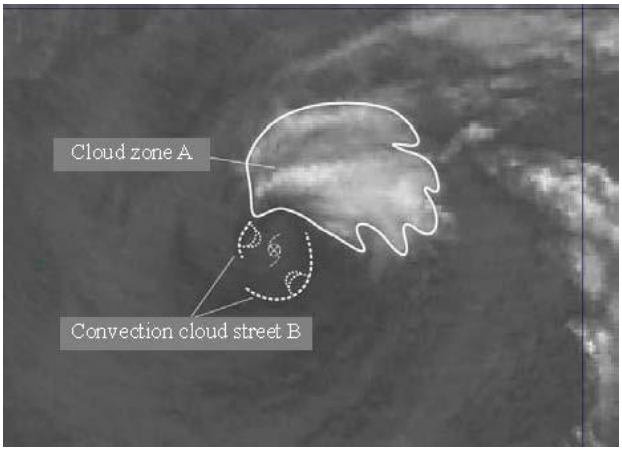

Figure 2-2b TC0004 89 GHz
Taken at 17UTC, June 8, 2005
Eye location: 26.6N 135.1E

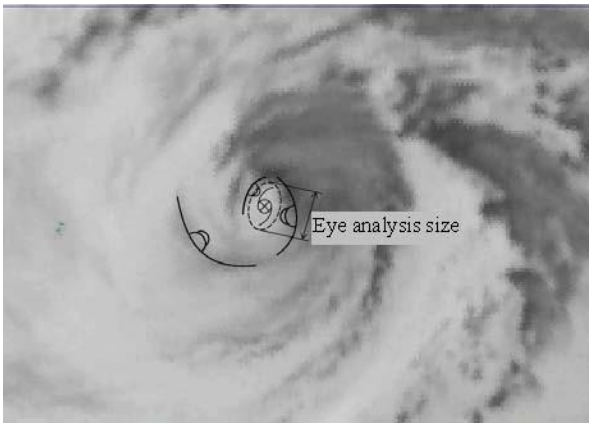

Figure 2-2c TC0004 36 GHz
Taken at 17UTC, June 8, 2005
Eye location: 26.6N 135.1E

clearness on 36-GHz imagery. To locate the eye, a cloud street that may suggest an eye, like convection cloud street C, is sought and the eye is located by locating the center of the circle of curvature (dotted line of the ellipse in Figure 2-2a) formed by the cloud street. As the eye analysis size, measure the length of the major axis of the circle of curvature.

Figure 2-2b shows a cloud pattern observed with the 89-GHz band. Cloud zone A is a cloud system of a tropical disturbance or a well-developed cloud zone of low brightness temperature. On the south side of this zone, convection cloud street B of high radiation temperature is observed. Cloud streets that may suggest the eye are shown by dotted lines. However, brightness temperature of the cloud streets is nearly the same as that of the sea surface, resulting in a low contrast between them. Therefore, they cannot be distinguished from the sea surface. The eye suggested from these streets is also shown. This is the candidate for the tropical disturbance eye.

In the 36-GHz imagery, the amount of microwaves emitted from the sea surface is small, so a convection cloud street is easily identifiable. Among convection cloud streets on the image, a combination of those that may suggest the eye is selected. An example of this is shown in Figure 2-2c. Using the calculated curvature of the clouds, the eye location is estimated. If this location is different from that in the 89-GHz imagery, use the figure of the 36-GHz imagery because its parallax error is smaller (final result). The length of the major axis of the circle of curvature (dotted line ellipse) formed by the selected convection cloud streets is measured as the eye analysis size.

b. EYE pattern

In microwave imagery, there are two possible cases: i. the complete-ring eye (Figure 2-3a), and ii. the incomplete-ring eye (Figure 2-4a). Even in the latter case, if a cloud band stretches at least halfway around the eye, the EYE pattern can be applied.

i Complete-ring eye

Figure 2-3a shows a schematic diagram of the “complete-ring EYE” pattern. A cloud zone takes the shape of a complete ring, which make eye analysis easy.

In an 89-GHz band image (Figure 2-3b), cloud zone A of low brightness temperature, which takes the shape of a ring, is the major characteristic of this pattern. The eye is in an area of high brightness temperature shown by a dotted line circle near the center of the cloud zone. The center of this area is defined as the eye (candidate). The eye analysis size is defined as the diameter of the eye or the major axis, so in this figure, the diameter of the dotted line circle is measured.

In the 36-GHz band image of Figure 2-3c, the eye is in an area of low brightness temperature in the central part of the cloud zone, and the center of this area is the eye of the disturbance. If the eye in the 36-GHz image is clearly seen, and differs in location from the eye in the 89-GHz image, the eye location in the 36-GHz band, which is less affected by parallax, is accepted as the eye of the disturbance (final result). If the eye in the 36-GHz image is unclear, the eye location in the 89-GHz image is accepted as the eye location of the disturbance. The eye analysis size is the diameter or major axis of the eye. In Figure 2-3c, the length of the major axis of the dotted-line ellipse is measured. This value is compared with that of the 89-GHz image, and a smaller one is accepted as the final eye analysis size.

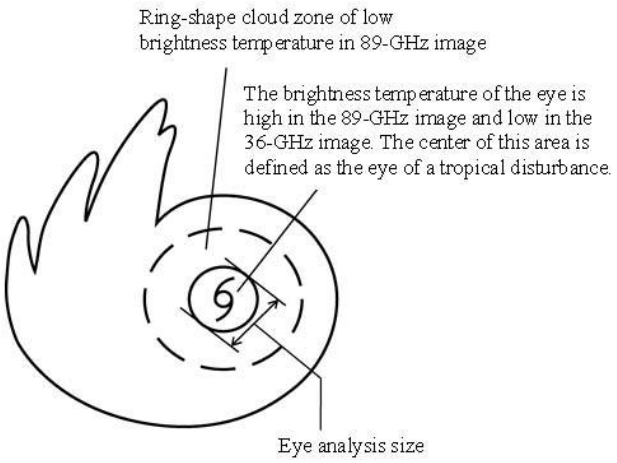

Figure 2-3a Pattern of complete-ring EYE

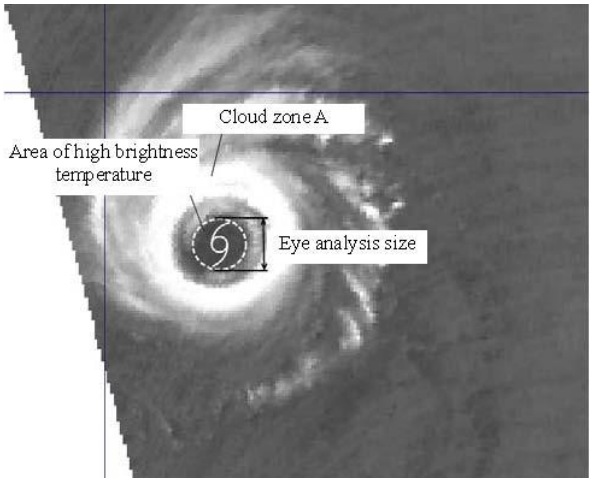

Figure 2-3b TC0003 89 GHz
Taken at 04UTC, April 13, 2004
Eye location: 17.5N 131.2E

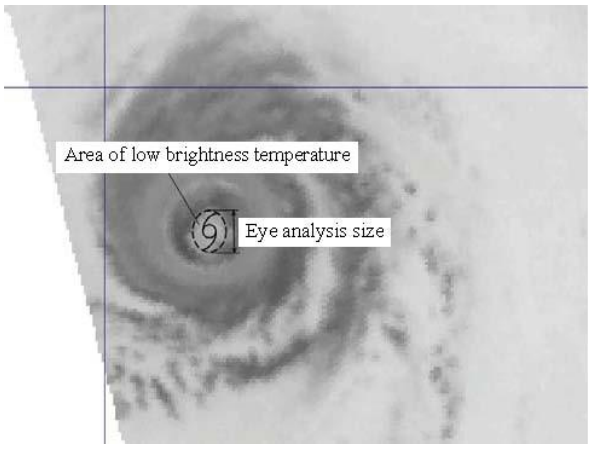

Figure 2-3c TC0003 36 GHz
Taken at 04UTC, April 13, 2004
Eye location: 17.5N 131.2E

ii Incomplete-ring eye

Figure 2-4a shows a schematic diagram of the "incomplete-ring EYE" pattern. Unlike the complete-ring pattern, the main characteristic of the pattern is that a cloud band does not form a complete ring, and is swirling. This pattern is often observed clearly in 89-GHz images and is often confused with the EYE pattern, which has an ambiguous ring structure in 36-GHz images.

An example of 89-GHz images is shown in Figure 2-4b. An area of low brightness temperature (cloud zone A) surrounded by a white solid line takes the shape of an "incomplete ring." Area B of high brightness temperature in the central portion of zone A is the eye. The center of this area is defined as the eye of the disturbance (candidate). The length of the major axis of the dotted-line ellipse is measured as the eye analysis size.

Figure 2-4c is a 36-GHz image in which the eye is an area of low brightness temperature (dotted-line ellipse) in the central portion of a cloud zone of high brighness temperature. The center of this eye is the eye of the disturbance. If the eye location is different between the 36-GHz and 89-GHz images, which is caused by parallax, the eye location of the 36-GHz image is accepted (final result). If the eye is not observed more clearly in the 36-GHz image than in the 89-GHz image, the eye location in the high-frequency image is accepted (the final result). The eye analysis size is the major axis of the eye (dotted-line ellipse). This value is compared with that of the 36-GHz image, and the smaller one is accepted as the final eye analysis size.

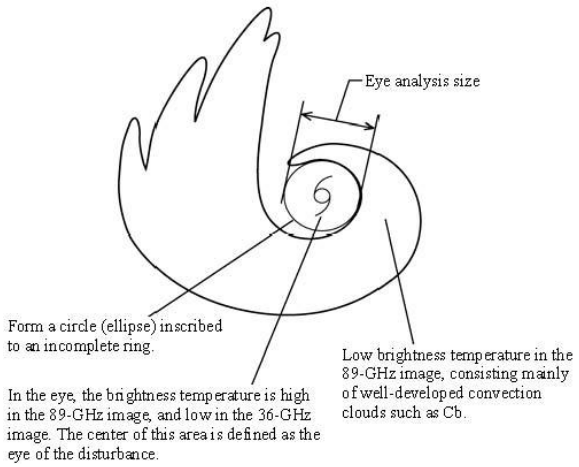

Figure 2-4a Incomplete-ring EYE pattern

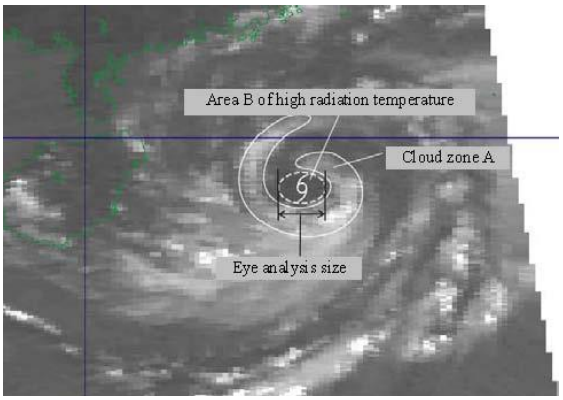

Figure 2-4b TC0006 89 GHz
Taken at 06UTC, Aug. 24, 2003
Eye location: 19.1N 113.7E

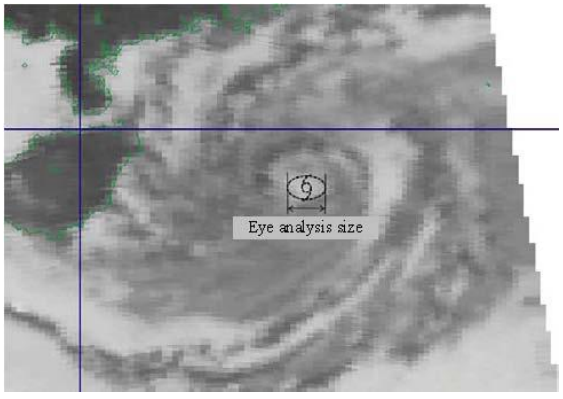

Figure 2-4c TC0006 36 GHz
Taken at 06UTC, Aug. 24, 2003
Eye location: 19.1N 113.7E

BAND pattern

In sharp contrast to the SHEAR pattern, in the BAND pattern, the eye of the disturbance is in a cloud system. In contrast to the EYE pattern, in the BAND pattern, no eye is formed or an arc is with its length being less than half that of a complete ring is formed due to in-progress formation. Compared with the SHEAR and EYE patterns, the BAND pattern has no clear convection cloud streets, and there are often scattered convection clouds. Before an eye analysis, it should be checked whether a cloud zone of low brightness temperature in an 89-GHz band image or one of high brightness temperature in a 36-GHz band image has a curvature that suggests an eye or takes the shape of a band.

Figure 2-5a shows a schematic diagram of the BAND pattern. Cloud zone A is a cloud system of a tropical disturbance, which does not always exhibit low brightness temperature in 89-GHz images. If it consists mainly of water clouds, the cloud system appears as a clear area of high brightness temperature in 36-GHz images. Convection cloud street B is a cloud street that suggests the eye in a tropical disturbance system. The circle of curvature formed by this cloud street is the eye of the disturbance. The length of the major axis of this circle is measured as the eye analysis size.

Figure 2-5b shows an 89-GHz image of the BAND pattern, in which cloud zone A surrounded by a dotted line shows the cloud system of a disturbance. In this example,

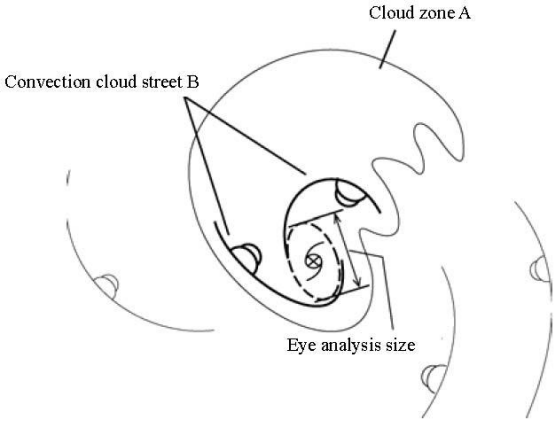

Figure 2-5a BAND Pattern

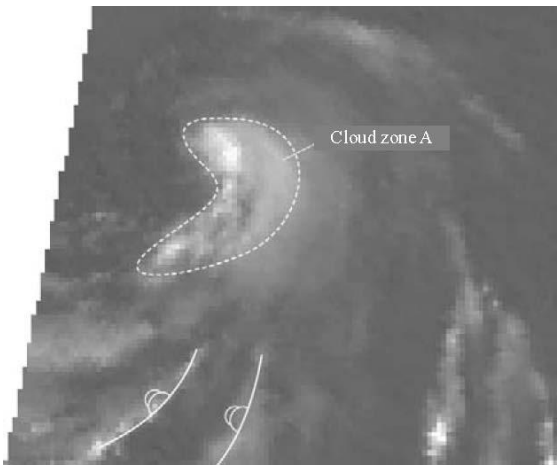

Figure 2-5b TC0008 89 GHz
Taken at 18UTC, June 11, 2004
Eye location: 13.7N 112.2E

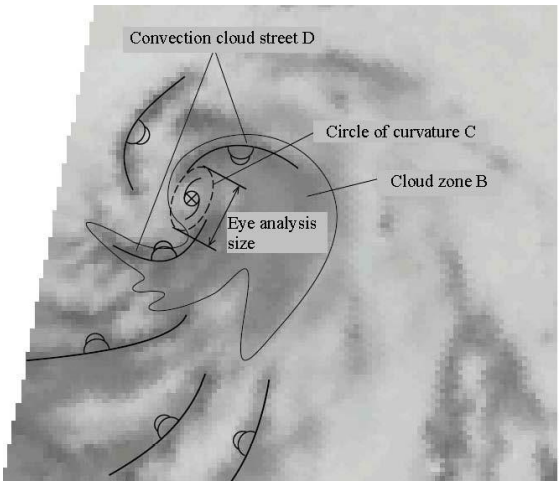

Figure 2-5c TC0008 36 GHz
Taken at 18UTC, June 11, 2004
Eye location: 13.7N 112.2E

clouds of low brightness temperature do not appear as dense cloud areas, and only a small portion of clouds in the image are sufficiently developed. In the image, the cloud system does not contain a cloud street that suggests the eye.

Figure 2-5c shows a 36-GHz image, in which cloud system B contains convection cloud street D that suggests the eye. The center of the circle of curvature C formed by this cloud street is the eye of the disturbance. The length of the major axis of this circle is measured as the eye analysis size.

2.7 Study results

The study results are described according to each item.

a. Pattern-specific occurrence rate using microwave imagery

In our study, the EYE pattern accounts for 57.3 percent of the total, suggesting an extremely high occurrence rate of the pattern (Figure 2-6).

Table 2-3 lists the combination occurrence rates of patterns of tropical disturbance in visible/infrared imagery and the pattern of microwave imagery for the same observation time. Analysis times for visible/infrared imagery and those for microwave imagery were compared, and the number of comparable cases was found to be 161. The time interval for analysis of visible/infrared imagery is 6 hours in the case of tropical cyclones that require issuance of gale warnings, and 3 hours in the case of typhoons. Both cases are included in our study. When the SHEAR pattern is found on visible/infrared imagery, the same pattern is frequently found on microwave imagery. However, concerning the other patterns on visible/infrared imagery, the EYE pattern is the majority pattern on microwave imagery. Unknown patterns found on microwave imagery are not listed because the analysis time was not the time for typhoon analysis, or data were rejected based on the quality control threshold value of a latitude/longitude error of more than 2 degrees, as described in Chapter 2.5.

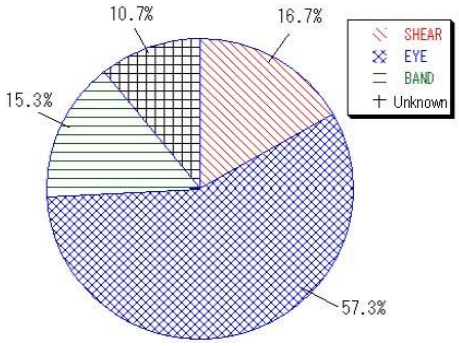

Figure 2-6 Pattern specific occurrence rates for a total of 466 cases

Table 2-3 Occurrence rates in a combination of patterns for visible/infrared and microwave imagery
IRVIS refers to infrared and visible. MW refers to microwave. Total, 161 cases
Each figure is the proportion of each MW pattern for each IRVIS pattern.

	IRVIS BAND	IRVIS B-EYE	IRVIS EMBED	IRVIS EYE	IRVIS SHEAR	IRVIS CB-Cluster
MW SHEAR	3.5	4.8	0.0	0.0	71.4	22.7
MW EYE	64.9	95.2	100.0	100.0	14.3	40.9
MW BAND	31.6	0.0	0.0	0.0	14.3	36.4

(Unit: %)

b. Analysis precision for tropical disturbance

i. Frequency distribution of eye distance

Figure 2-7 shows occurrence rates of eye distances between visible/infrared and microwave imagery based on the eye pattern.

In this figure, the rate columns of all types are piled up into a single column, as shown in the figure. No data are available for unknown patterns on microwave imagery because no eye analysis is performed on these patterns. The chart shows the highest frequency of distances of not less than 20 and less than 30 kilometers. The longer the eye distance, the less the frequency. Eye distances of not less than 100 kilometers account for 2.5 percent.

The occurrence rates of the EYE pattern are high at an eye distance of not more than 100 kilometers.

Figure 2-8 shows the occurrence rates of eye distances between RADOB reports and microwave imagery based on the eye pattern.

In RADOB reports, if a disturbance is observed at more than one radar site, data are reported by site. Even if more than one radar caught the same disturbance, we use both data. Times that match those of microwave imagery are extracted, so that a total of 71 cases are prepared. The results show the same tendency for eye distance between visible/infrared and microwave imagery (Figure 2-7). However, concerning the eye distance between visible/infrared and microwave imagery:

- The highest occurrence rate at a distance of not less than 20 to less than 30 kilometers.

  And concerning the eye distance between microwave imagery and RADOB reports:

- The highest occurrence rate at a distance of not less than 10 to less than 20 kilometers.

The eye difference between visible/infrared and microwave imagery is smaller than that between microwave imagery and RADOB reports, which suggests a higher precision of comparison with RADOB reports. Based on its analytical precision, results of comparison with RADOB data are also

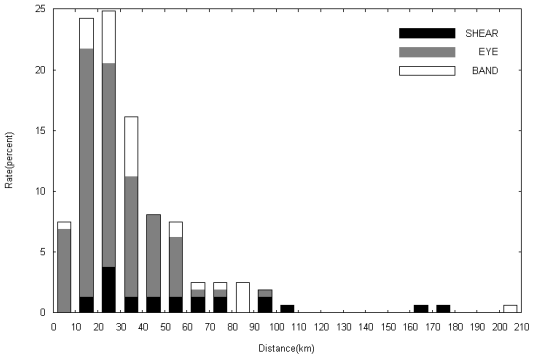

Figure 2.7 The horizontal axis indicates the eye distance between visible/infrared and microwave imagery. The vertical axis indicates the occurrence rate. Total, 161 cases

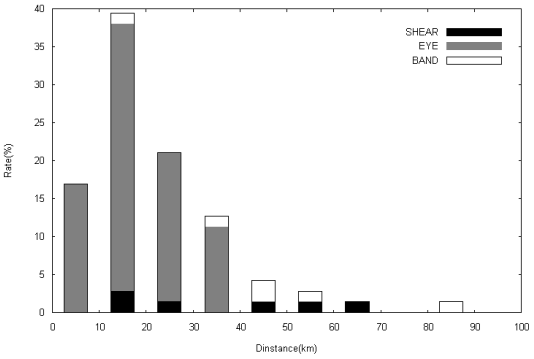

Figure 2-8 The horizontal axis indicates the eye distance between microwave imagery and RADOB reports. The vertical axis shows the occurrence rate. Total, 71 cases

acceptable.

ii. Latitude/longitude error distribution

Figure 2-9 shows the distribution of tropical disturbance eyes on visible/infrared imagery based on tropical disturbance eyes on microwave imagery. The distribution is created by plotting a value gained by subtracting (the microwave eye location) from (the visible/infrared eye location) on each latitude and longitude. Within ± 0.3 degrees, 66 percent of the data are distributed. Figure 2-10 is prepared by plotting a value gained by subtracting (the microwave eye location) from (the RADOB eye location) on each latitude and longitude. Within ± 0.3 degrees, 80 percent of the data are distributed. Errors of not less than one (1) degree are not observed in Figure 2-10, but are observed in Figure 2-9. These errors are produced because "off-target" analyses on eye location were performed. The use of microwave imagery can decrease the number of such errors.

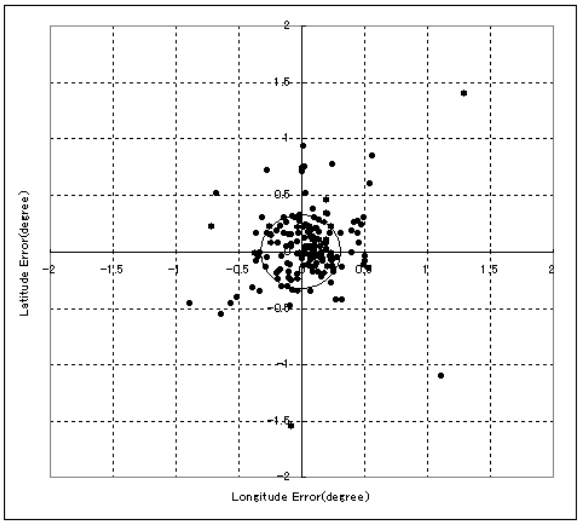

Figure 2-9 Scatter diagram of eye location of visible/infrared imagery based on microwave imagery
The origin is the eye location of disturbance on microwave imagery. Plotted data show eye locations on visible/infrared imagery. The circle has a diameter of 0.3 degrees. Total, 161 cases

c. Comparison between microwave and visible/infrared imagery

Figure 2-11 shows comparison between accuracy (eye precision) in visible/infrared imagery and eye analysis size in microwave imagery. For visible/infrared imagery, a range of 40 to 60 kilometers is observed frequently, while a range of 20 to 40 kilometers is observed frequently for microwave imagery. This means that it is easier to locate the eye of a disturbance using microwave imagery.

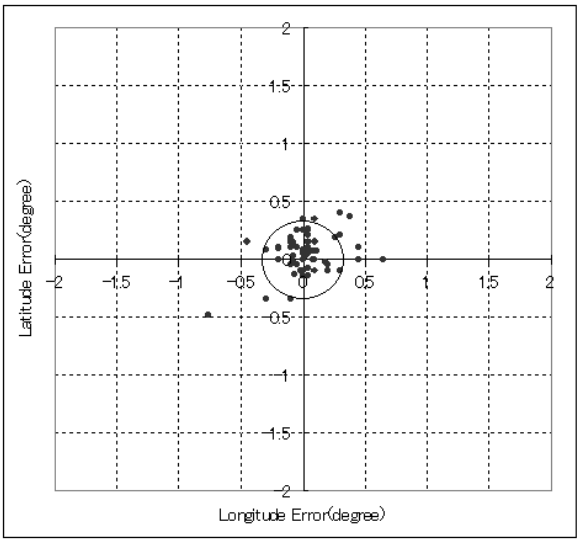

Figure 2-10 Scatter diagram of eye location of RADOB data based on microwave imagery
The origin is the eye location of disturbance on microwave imagery. Plotted data show eye locations on RADOB reports. The circle has a diameter of 0.3 degrees. Compared with Figure 2-8, the data are less scattered. Total, 71 cases

On the assumption that eye locations of

RADOB reports are correct, the probability that the eye distance between microwave imagery and RADOB reports is not more than the eye analysis size is 92 percent. This means that within the area of the eye analysis size of microwave imagery, there are 92 percent of the eyes on RADOB reports. The eye analysis size carries nearly the same meaning as that for accuracy (eye precision) for visible/infrared imagery.

Figure 2-12 shows the comparison results of the imagery type for an operator to analyze a tropical disturbance with ease between microwave and visible/infrared. Items of "Microwave imagery is clearer" and "Microwave imagery is slightly clearer" account for more than 50 percent of the total. This means that operators could analyze disturbance eyes more easily using microwave imagery. As an example, Figure 2-13 shows an image of TC0007 taken at 18UTC, June 6, 2004. At that time, a gale warning was issued, but a typhoon was not generated. The Analysis Division of the Meteorological Satellite Center was conducting an early-stage Dvorak analysis. The organized Cb cluster pattern is used for traditional operational analysis using visible/infrared imagery. Because of dense high-altitude clouds across an image, it is difficult to locate an eye without seeing a moving image. In microwave imagery, an at least one half of a ring of cloud is observed in an 89-GHz image, and a complete ring of cloud is observed in a 36-GHz image. The pattern is the microwave EYE pattern. As this example shows, eye analysis work is easier using microwave imagery.

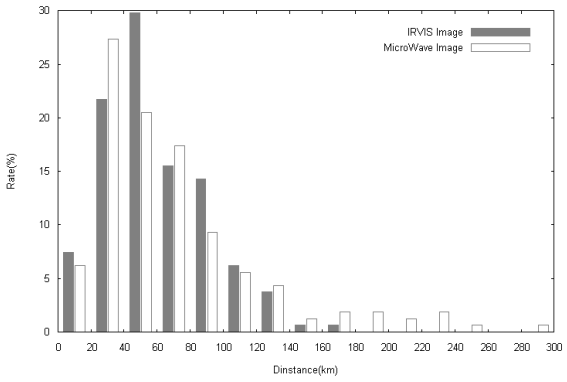

Figure 2-11 Occurrence rates of accuracy (eye precision) for visible/infrared imagery and eye analysis size for microwave imagery for intervals of 20 kilometers Total, 161 cases

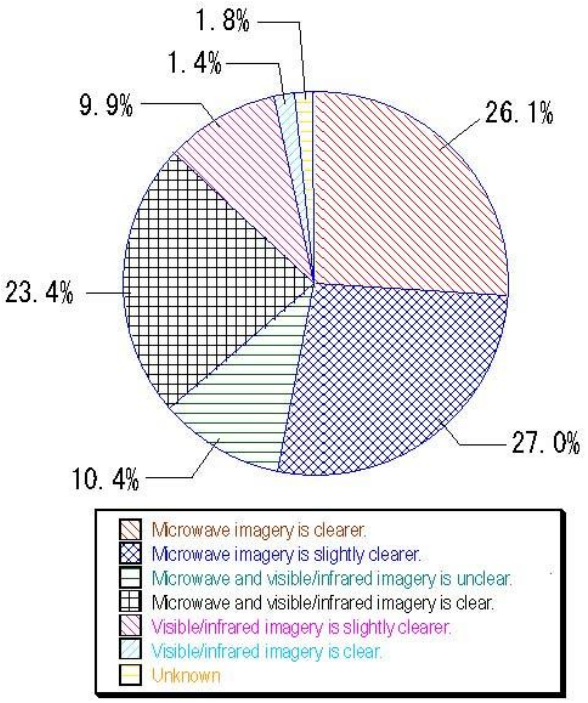

Figure 2-12 Comparison of ease of eye analysis work

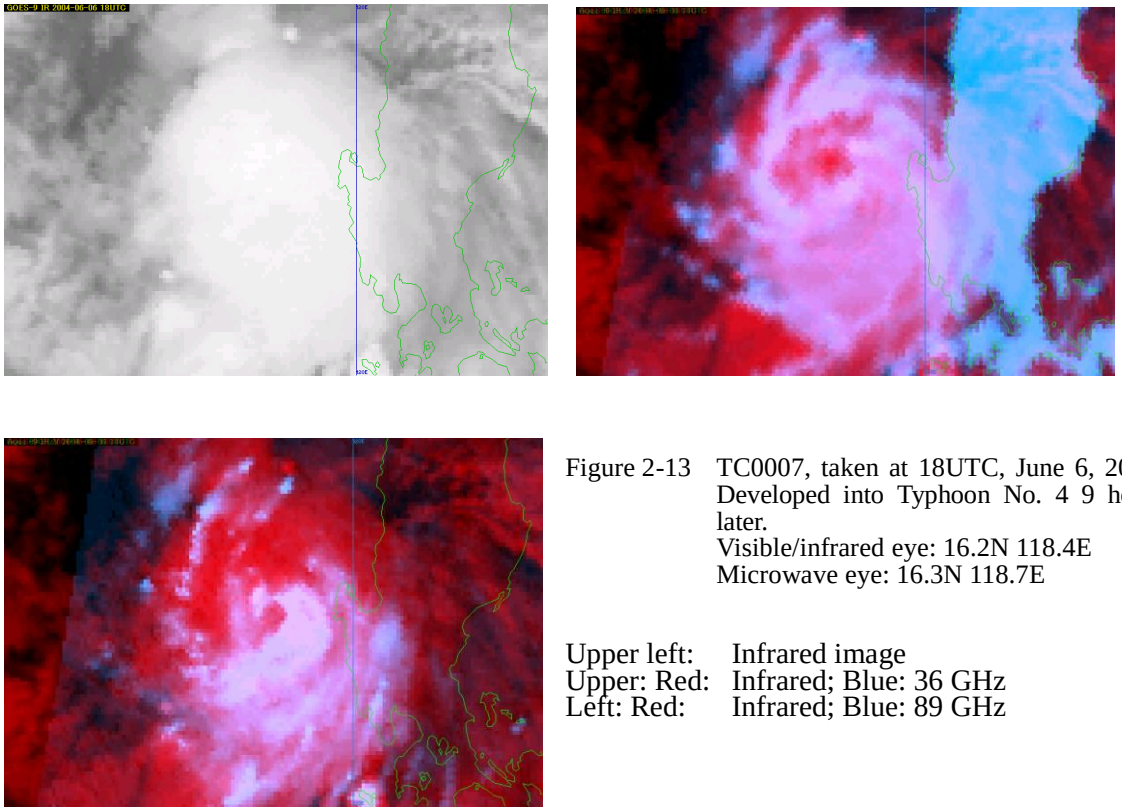

Figure 2-13 TC0007, taken at 18UTC, June 6, 2004. Developed into Typhoon No. 4 9 hours later.
Visible/infrared eye: 16.2N 118.4E
Microwave eye: 16.3N 118.7E

Upper left: Infrared image
Upper: Red: Infrared; Blue: 36 GHz
Left: Red: Infrared; Blue: 89 GHz

2.8 Discussion

a. Observation frequency per day

A problem of tropical disturbance analysis using microwave imagery is the low frequency of observation. Satellite MTSAT-1R observes the northern hemisphere of the earth twice an hour, which comes to 48 times in 24 hours. Satellite AMSR-E observes an area at a longitude of 100 to 180 degrees about 8 times per day. Because of its low swath width, approximately 1400 kilometers, the number of times that the satellites passes over a tropical disturbance with a size of approximately 1000 kilometers is very small, producing a small number of images taken. This problem can be solved by using many data obtained with polar orbiting satellites; however, at the present, in the number of observation times, a geostationary meteorological satellite, which can observe an object twice an hour and whose moving images can be used for eye analyses, compares favorably with the microwave satellite.

b. Resolution

The resolution of Satellite MTSAT-1R is 4 kilometers on infrared imagery and 1 kilometer on visible imagery. The resolution of AMSR-E is 5 kilometers for the 89-GHz band, and 11 kilometers for the 36-GHz band. In resolution, the latter satellite compares unfavorably with the former.

c. Pattern classification

Selection between the SHEAR and BAND patterns depends frequently on the operator. The BAND pattern is selected if a phenomenon is not classified into the SHEAR or EYE pattern. Because it is passively selected, adoption of the BAND pattern depends on an operator who judges the possibility of analysis using the SHEAR pattern. It is a future task to define the BAND pattern more clearly.

d. Eye analysis precision

As described in Chapter 1, a cloud zone observed with the AMSR-E sensor that uses a conical scan mode has a certain degree of parallax with respect to the ground surface. In our study, to reduce this difference to the extent possible, the final result of eye location is determined using 36-GHz images, which are lower in parallax than 89-GHz images. However, 36-GHz images still have some degree of parallax, and this fact should be kept in mind during eye analysis using microwave imagery.

On the assumption that eye locations in RADOB reports are reliable, eye locations identified using microwave imagery are more precise than those using visible/infrared imagery, according to our study results. The eye distance between RADOB reports and microwave imagery is found to be at least 10 and less than 20 kilometers with high frequency, and less than 10 kilometers with low frequency. These margins of error are unavoidable in the analytical results of microwave imagery.

d. Automation of eye analysis

According to our study, in comparison with visible/infrared imagery, on microwave imagery, the EYE pattern is more frequently observed, and an eye analysis is easier. It seems that this fact is advantageous only when an operator conducts an eye analysis on the man-machine interface. A cloud of a ring of low or high radiation temperature that clearly suggests the eye is useful for automatically locating eyes using software applications.

e. Observation site for three patterns for microwave imagery

Because in our study, eye analyses are performed on all of the three patterns, excluding unknown patterns, whether observation points have any unique characteristics for each pattern is checked, which found no major difference. In order to observe the generation of a tropical disturbance at an earlier stage, information on sites of tropical disturbance generation is important, which we have not studied. This merits further research.

2.9 Summary

When a tropical disturbance is observed on microwave imagery, the occurrence rate of the EYE pattern accounts for 60 percent of the total, which shows that it is the majority pattern among all. Many patterns other than the EYE pattern on visible/infrared imagery are found to be the EYE pattern on microwave imagery. Concerning eye analysis precision using microwave imagery, eye locations analyzed using microwave imagery are found to be approximate values of RADOB reports. An eye

analysis using microwave imagery is found to be more precise than that using only visible/infrared imagery.

References

Norihisa Usui, Yukio Kurihara and Akiko Shoji, 2003: QuikSCAT Verification Study and Objective Analysis using the Variation Method on Ocean Winds, Weather Service Bulletin, 70.2, P25-39.

Koji Kato, Makoto Nishida, Masayuki Yamamoto, Naoyuki Shimizu and Akihiro Kikuchi, 2004: Tropical Disturbance Analysis System, Meteorological Satellite Center Technical Note No. 44, Meteorological Satellite Center, P31-38.

Shuji Nishimura, 2006: 2-9 Tropical Disturbance Analysis, 2006 Special Issue of Meteorological Satellite Center Technical Note Comprehensive Report of MSC System, Meteorological Satellite Center, P145-153.

Tadahiro Hayasaka (ed) 1996: Remote Sensing of the Atmosphere Using Microwave Radiometry, Meteorological Study Note, 187, PP196.

Masaya Hirohata, 2004: Chapter 5 Use Various Types of Satellite Data, Analyze and Use Meteorological Satellite Images --Tropical Cyclones--, Meteorological Satellite Center, P102-107.

Yukio Fujita and Takeshi Hagiwara, 2000: Chapter 1 Meteorological Satellite Observation of Typhoons, Meteorological Study Note, 197, P1-75.

Grody, N. C., 1993: Remote Sensing of the Atmosphere from Satellite Using Microwave Radiometry, Atmospheric Remote Sensing by Microwave Radiometry (eds. M. A. Janssen), John Wiley & Sons, New York, P37-90.

Kidder, Stanley Q., Mitchell D. Goldberg, Raymond M. Zehr, Mark DeMaria, James F. W. Purdom, Christopher S. Velden, Norman C. Grody, and Sheldon J. Kusselson, 2000: Satellite Analysis of Tropical Cyclones Using the Advanced Microwave Sounding Unit (AMSU), Bulletin of the American Meteorological Society, 81, 1241-1259.

Lee, Thomas F., Francis J. Turk, Jeffrey Hawkins, and Kim Richardson, 2002: Interpretation of TRMM TMI Images of Tropical Cyclones, Earth Interactions, 6, P1-17.

NASA, 1987: High Resolution Multi-frequency Microwave Radiometer, Earth Observing System Volume IIe, Instrument Panel Report, NASA, Washington D.C., P59.

Randall J. Alliss, Sethu Raman and Simon W. Chang, 1992: Special Sensor Microwave / Imager (SSM/I) Observations of Hurricane Hugo (1989), Monthly Weather Review, 120, P2723-2737.

Randall J. Alliss, Glenn D. Sandlin, Simon W. Chang and Sethu Raman, 1993: Applications of SSM/I Data in the Analysis of Hurricane Florence (1988), Journal of Applied Meteorology, 32, P1581-1591.

Spencer, Roy W., H. Michael Goodman, Robbie E. Hood, 1989: Precipitation Retrieval over Land and Ocean with the SSM/I: Identification and Characteristics of the Scattering Signal, Journal of

Atmospheric and Oceanic Technology, 6, 254-273.

Appendix 1 Satellites and Sensors

The following is a description of abstracted, revised and edited information about satellites and sensors provided from the appendix of separate report No. 53 of the Numeric Prediction Division.

- The following satellites and sensors are relevant to our report, and do not cover all sensors loaded on to the satellites.
- Shaded areas are concerned with satellites that have not been launched and may be subject to their program review or change in the future.
- Abbreviations in the tables are as follows: IR: Infrared; MW: Microwave; VIS: Visible; VN: Visible-Near infrared; SW: Short wavelength infrared; WV: Water vapor channel of stationary satellite; -S: Sounder; -I: Imager; -IS: Imager/sounder; and -HS: Hyperspectral sounder.
- Measurement precision is generally based on radiation temperature in the unit of K. If quantitation precision (bit) or signal-noise ratio (S/N) is required, a value and the unit are stated in each case.
- Figures in braces in the Precision or Application field present appropriate ranges of precision.
- Some fields are filled with a bar because of "Not applicable," "To be determined because of contemplation" or "Insufficient information."
- Abbreviations in the Wavelength & Frequency field represent the following: V: Vertical; H: Horizontal; L: Left; R: Right; +45: +45 degree polarization; and -45: -45 degree polarization. To show only the number (n) of polarization states, add "Pn" before a figure. None of these symbols in a field shows that polarization is not classified.
- To show the number of bands, add [B] before a number.
- To show vertical resolution, add [V] before a number.

Name of satellite series or program	Satellite name	Sensor name	Sensor type	Wavelength [μm] Frequency [GHz]	Number of channels	Measure-ment precision [K]	Spatial resolution [km]	Application	Launch date (other information)
GeoStationary Satellite									
MTSAT Japan	MTSAT-1R	JAMI	IR_VIS-I	[VIS] 0.55-0.90 [IR] 10.3-11.3 11.5-12.5 6.5-7.0 3.5-4.0[μm]	5	[VIS] 6.5 {2.5% albedo} [IR1] 0.18 [IR2] 0.18 [IR3] 0.15 [IR4] 0.18 {300K}	[VIS] 1 [IR] 4	Cloud distribution/ wind	Feb. 2005
	MTSAT 2	IMAGER	IR_VIS-I	[VIS] 0.55-0.90 [IR] 10.3-11.3 11.5-12.5 6.5-7.0 3.5-4.0[μm]	5	[VIS] 6.5 {2.5% albedo} [IR1] 0.09 [IR2] 0.12 [IR3] 0.11 [IR4] 0.20 {300K}	[VIS] 1 [IR] 4	Cloud distribution/ wind	Feb. 2006

Name of satellite series or program	Satellite name	Sensor name	Sensor type	Wavelength [μm] Frequency [GHz]	Number of channels	Measure-ment precision [K]	Spatial resolution [km]	Application	Launch date (other information)
Polar Orbiting Satellite, and others									
CloudSat U.S. (NASA) Canada (CSA)	CloudSat	CPR	Cloud radar	94[GHz]	1	Calibration precision 1.5[dB]	2, [V]0.5	Three-dimensional distribution of clouds	Apr. 2006
DMSP U.S. (air force)	DMSP F13 14 15	SSM/I	MW-I	19.35VH 22.24V 37.0VH 85.5VH[GHz]	7	0.6	69×43	Atmospheric temperature, water vapor (vertical) distribution, precipitable water, precipitation intensity [5mm/hr], ocean surface wind speed [2m/s]	Mar. 1995 Apr. 1997 Dec. 1999
						0.6	60×40		
						0.6	37×28		
						1.1	15×13		
		SSM/T1	MW-S	50.5 -59.4[GHz]	7	-	Diameter 174		
		SSM/T-2	MW-S	91.5, 150,183[GHz]	5	0.45	48		
	F16	SSMIS	MW-IS	19.35VH	24	0.35	46.5×73.6	(cont.) Sea surface temperature [2K], sea-ice distribution, ice concentration, snow cover, and solid moisture distribution	Oct. 2003
	17			22.235V		0.45	46.5×73.6		Nov. 2006
	18			37VH		0.22	31.2×45.0		Oct. 2007
	19			91.655VH		0.19	13.2×15.5		Apr. 2009
	20			60,63		0.38-1.23	75.2×75.0-37.7-38.8		Oct. 2011
				50.3-59.4H		0.20-0.26	37.7×38.8		
				150H		0.53	13.3×15.5		
				183H[GHz]		0.38-0.56	13.2×15.5		

Name of satellite series or program	Satellite name	Sensor name	Sensor type	Wavelength [μm] Frequency [GHz]	Number of channels	Measure-ment precision [K]	Spatial resolution [km]	Application	Launch date (other information)
EOS U.S. (NASA)	Aqua	MODIS	IR_VIS-I	0.4-14.4 [μm]	36	0.05(300K)	0.25, 0.5, 1	Clouds, ground information, SST, sea-ice ratio, wind	May 2002
		AMSR-E	MW-I	6.925 VH, 10.65 VH, 18.7 VH, 23.8 VH, 36.5 VH, 89.0 VH [GHz]	12	0.3 0.6 0.6 0.6 0.6 1.1	74×43 51×30 27×16 32×18 14×8 6×4	Precipitable water, sea surface wind speed, sea surface temperature, sea-ice distribution and soil moisture distribution	
		AMSU-A	MW-S	Same as NOAA					
		HSB	MW-S	150,183[GHz]	4	-	13.5km	Vertical distribution of amount of water vapor	
		AIRS	IR-HS	649-1135, 1217-1613, 2169-2674[1/cm]	2378	0.15-0.35	13.5	Atmospheric temperature, vertical distribution of amount of water vapor, land/sea surface temperature, cloud characteristics, and radiation energy flux	
		CERES	Net radiometer	0.3-5, 8-12 ,0.3-50[μm]	3	Shortwave radiation 2% Longwave radiation 1%	21km	Radiation balance	
	Terra	MODIS	IR_VIS-I	Same as Aqua					Dec. 1999
		ASTER	VIS_IR-I	0.5-0.9	3	8[bit]	15m	Clouds, land usage, sea surface temperature	
				1.6-2.5	6	8[bit]	20m		
				8-12[μm]	5	0.3, 12[bit]	90m		
		MISR	Multidirectional radiometer	0.45,0.56, 0.57,0.87[μm]	4	-	0.24,0.48, 0.96,1.92	Albedo, aerosol	
		MOPITT	Tropospheric contamina-tion monitor	2.2-4.7[μm]	8	-	22×22	Tropospheric contamination monitoring	
		CERES	Net radiometer	Same as Aqua					
	Aura	OMI	Atmospheric chemical sensor	0.350－0.5, 0.270－0.314, 0.306－0.38 [μm]	-	Spectral resolution 1.0-0.45[nm]	13×25	Ozone distribution [1-5%]	Jul. 2004
		TES	Tropospheric radiometric spectrometer	2.3-15.4[μm]	-	Spectral resolution 0.025-0.1[1/cm]	0.53×5.3	Chemical distribution	
		HIRDLS	Sounder for peripheral observation	6.12-17.76[μm]	21	-	500,[V]1	Chemical distribution	
		MLS	MW rim sounder	118, 190, 240, 640, 2500[GHz]	5	Spectral resolution 5[MHz]	5 ×500	Amount of water vapor in upper convection sphere	

Name of satellite series or program	Satellite name	Sensor name	Sensor type	Wavelength [μm] Frequency [GHz]	Number of channels	Measure-ment precision [K]	Spatial resolution [km]	Application	Launch date (other information)
GCOM-W Japan (JAXA)	GCOM-W1 -W2 -W3	AMSR2	MW-I	6.925VH 7.3VH 10.65VH 18.7VH 23.8VH 36.5VH 89.0VH [GHz]	14	0.34 0.7 0.7 0.6 0.7 1.2	35×62 24×42 14×22 15×26 7×12 3×5	Precipitable water, precipitation intensity, sea surface wind speed, sea surface temperature, sea-ice distribution, ice concentration, snow cover, and soil moisture distribution	Three satellites are planned to be launched every four years starting around 2011-2012
GCOM-C Japan (JAXA)	GCOM-C1 -C2 -C3	SGLI	IR_VIS-I	[VN]380-565 670P3, 865P3 [nm] [SW]1050-2210 [nm] [T]10.8,12.0 [μm]	[B] 19	12[bit]	[VN] 0.25-1 [P] 1 [SW] 0.25-1 [T] 0.5	Observation of atmospheric and ground conditions relevant to carbon cycle and radiation balance	Three satellites are planned to be launched every four years starting around 2012-2013
GOSAT Japan	GOSAT	TANSO-FTS	Infrared spectrometer	0.76,1.6, 2.0,6-15[μm]	[B]4	Spectral resolution 0.2[1/cm]	10.5	Carbon dioxide level (1%)(4 ppmv)	Aug. 2008
		TANSO-CAI	IR_VIS-I	0.38,0.67, 0.87,1.62[μm]	4	Spectral resolution 20-90[nm]	0.5-1.5	Cloud and aerosol distributions	
GPM Japan and U.S.	Main GPM satellite	DPR	2-Frequency precipitation radar	13.6,35.5[GHz]	2	-	-	Precipitation	2013 [observation system consisting of one main satellite and eight sub-satellites]
		GMI	MW-I	10.7,19.3,21,37, 89,165, 183[GHz]	-	-	-	Cloud and precipitation characteristics	

Name of satellite series or program	Satellite name	Sensor name	Sensor type	Wavelength [μm] Frequency [GHz]	Number of channels	Measure-ment precision [K]	Spatial resolution [km]	Application	Launch date (other information)
NOAA U.S. (NOAA)	NOAA15 16 17	HIRS/3	IR-S	069, 3.76-4.57, 6.72-14.95[μm]	20	13[bit]	20.4	Vertical distributions of atmospheric temperature and amount of water vapor	May 1998 Sep. 2000 Jun. 2002
		AMSU-A	MW-S	23.8, 31.4, 89.0, 50.3-57.3[GHz]	15	0.25-1.20	48	Vertical distribution of atmospheric temperature	
		AMSU-B	MW-S	89.0, 150.3 183 [GHz]	5	0.37-1.06	16	Vertical distribution of amount of water vapor	
		AVHRR/3	IR_VIS-I	[VIS] 0.58-0.68 [IR] 0.725-1.1,1.6, 3.55-3.93, 10.3-11.3, 11.4-12.4[μm]	6	10[bit] 0.12	1.1	Cloud distribution, discrimination between snow and ice, and sea surface temperature	(Note: SBUV/2 will be loaded onto successor satellites to NOAA16)
		SBUV/2	Atmospheric chemical sensor	0.252-0.34 [μm]	12	14[bit]	170	Vertical distribution of ozone [1-5%]	
	NOAA18	HIRS/4	IR-S	069, 3.76-4.57, 6.72-14.95[μm]	20	13[bit]	10.2	Same as HIRS/3	May 2005
	NOAA N'	MHS	MW-S	89.0,157, 183, 190[GHz]	5	0.22-0.51	16	Same as AMSU-B	Dec. 2008
		AMSU-A SBUV/2 AVHRR/3	See information about NOAA15-17						

Name of satellite series or program	Satellite name	Sensor name	Sensor type	Wavelength [μm] Frequency [GHz]	Number of channels	Measure-ment precision [K]	Spatial resolution [km]	Application	Launch date (other information)
QuikSCAT U.S. (NASA)	QuikSCAT	SeaWinds	MW Wave scattering monitor	13.4[GHz]	1	-	25	Sea surface wind (RMSE 2[m/s]{3-20m/s} 20[deg])	Jun. 1996
TRMM Japan (NASDA) U.S. (NASA)	TRMM	TMI	MW-I	10.7VH, 19.35VH, 21.3V, 37.0VH, 85.5VH [GHz]	9	V/H 0.63/0.54 0.50/0.47 0.71 0.36/0.31 0.52/0.93	73×42 35×21 31×21 18×11 8×5	Precipitable water, sea surface wind speed, sea surface temperature, sea-ice distribution, and soil moisture distribution	Nov. 1997
		PR	Precipitation radar	13.796, 13.802 [GHz]	-	-	4.3 [V] 0.25	Three-dimensional precipitation distribution (0.7 mm/hr)	
		VIRS	IR_VIS-I	0.63, 1.6, 3.75, 10.8, 12.0 [μm]	5	-	2	Cloud distribution, and estimation of precipitation	
		CERES	Net radiometer	0.3-5, 8-12 , 0.3-50[μm]	3	Shortwave radiation 2% Longwave radiation 1%	21km	Radiation balance	

Reference URLs
http://www.restec.or.jp/databook/
http://www.data.kishou.go.jp/satellite/satellite.html
http://www.ipo.noaa.gov/ams/index.html
http://www.esa.int/esaCP/index.html
http://www.nasa.gov/